[AMERICAN JOURNAL OF SCIENCE, VOL. 299, APRIL, 1999, P. 309–339]

TECTONOTHERMAL EVOLUTION OF THE MAYUAN ASSEMBLAGE IN THE CATHAYSIA BLOCK: IMPLICATIONS FOR NEOPROTEROZOIC COLLISION-RELATED ASSEMBLY OF THE SOUTH CHINA CRATON

GUOCHUN ZHAO and PETER A. CAWOOD
Tectonics Special Research Centre, School of Applied Geology, Curtin University of Technology, GPO Box U1987, Perth, Western Australia 6845

ABSTRACT. The Mayuan assemblage in the Cathaysia Block, Southeast China, consists of felsic paragneiss, pelitic schist, greenschist, amphibolite, marble, calcsilicate, and quartzite that underwent three episodes of deformation (D_1-D_3) and four episodes of metamorphism (M_1-M_4) in the early Neoproterozoic. The M_1 assemblage consists of mineral inclusions defining an early foliation (S_1) within porphyroblasts, represented by chlorite + muscovite + biotite + plagioclase + quartz in pelitic schist and actinolite + chlorite + epidote + albite ± quartz enclosed in amphibolite. M_2 coincides with the development of the regional schistosity (S_2) and represents the formation of the porphyroblasts and growth of matrix minerals, resulting in development of prograde metamorphic zones (chlorite-biotite, garnet, staurolite, and kyanite zones). M_3 is simultaneous with the third phase of deformation (D_3) and produced sillimanite-bearing mineral assemblages in pelitic schist and hornblende-bearing assemblages in amphibolite. The last metamorphic episode M_4 gave rise to the retrogressive assemblage chlorite + muscovite in pelitic rock and actinolite + chlorite + epidote in amphibolite. The sequence of mineral assemblages and history of metamorphic reactions built from the petrogenetic grid of pelites suggest a near-isothermal decompression clockwise P–T path for the Mayuan pelitic schists. Using the TWEEQU software program, the garnet–biotite thermometer and garnet–muscovite–biotite–plagioclase barometer yield P–T conditions for M_1 of 5.5 to 6.0 kb and 450° to 500°C and conditions for the garnet, staurolite, and kyanite zones of M2 of 6.0 to 7.0 kb and 550° to 600°C, 6.0 to 7.5 kb and 600°C and 11.0 to 11.5 kb and 600°C. The P–T conditions of M_3 were estimated at 570° to 625°C and 4.0 to 4.5 kb using the muscovite-biotite thermometer and hornblende-plagioclase geothermobarometer. The garnet-chlorite thermometer yields temperatures of 300° to 400°C for M4, but the pressures of M_4 cannot be quantitatively estimated because of the lack of a suitable geobarometer. These P–T estimates also define an near-isothermal decompression clockwise P–T path, which is involved in initial crustal thickening followed by rapid exhumation and final cooling, and is related to amalgamation of the Cathaysia and Yangtze Blocks to form the South China craton.

INTRODUCTION

The South China craton consists of the Yangtze and Cathaysia Blocks lying to the northwest and southeast respectively of the Jiangshan-Shaoxing Fault (fig. 1). Models for the evolution of the craton range from those invoking an autochthonous relationship, with the two blocks developing on a common basement and the Cathaysia Block representing a continental marginal arc fold belt to the Yangtze Block (Huang, 1977; Dong, 1986; He and Zhang, 1989), to those proposing that they represent separate exotic terranes that collided along the Jiangshan-Shaoxing Fault (Shui, 1987; Hsü and others, 1988, 1990; Jahn, Zhou, and Li, 1990; Chen and others, 1991; Xu, 1992; Zhao, Sun, and He, 1994a; Li, Zhang, and Powell, 1995, 1996; Zhao and Sun, 1996). These models were based primarily on regional lithological and structural studies combined with limited geochemical and isotopic data, and few metamorphic studies have been undertaken on the major lithotectonic units within the two blocks.

Much of the recent research in metamorphic petrology has shown that modern field- and thermodynamics-based metamorphic investigations, in combination with lithological, structural, and geochronological considerations, can be directed toward

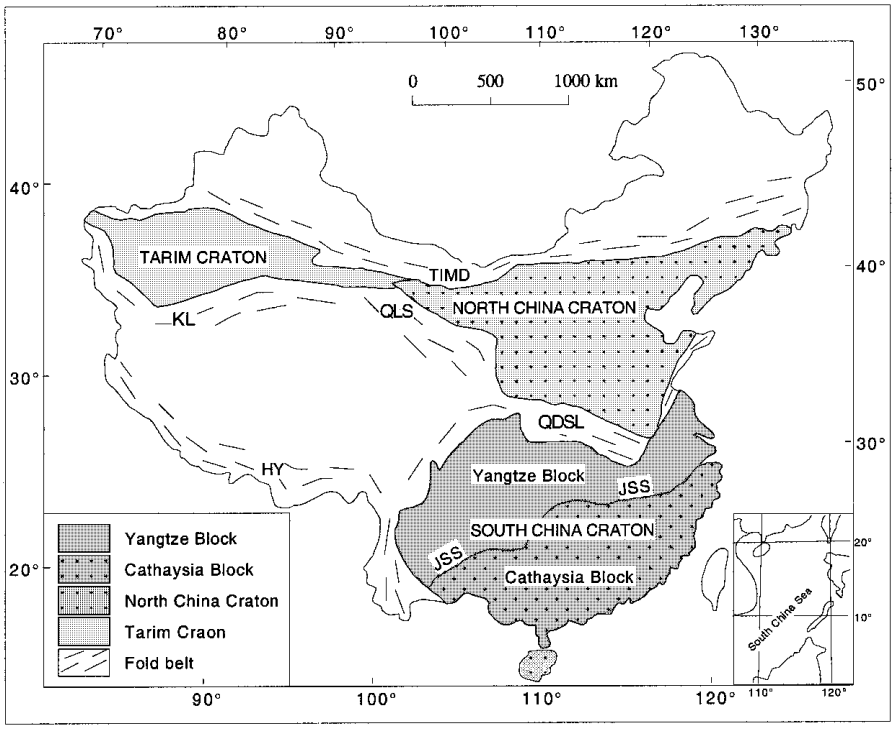

Fig. 1. Outline tectonic map of China showing the major Precambrian blocks and the Late Neoproterozoic and Paleozoic fold belts. HY–Himalaya fold belt; KL–Kunlun fold belt; JSS–Jiangshan-Shaoxing suture; QDSL–Qinlin–Dabie–Su–Lu fold belt; QLS–Qiliansham fold belt; TIMD–Tianshan–Inner Mongolia–Daxinganling fold belt.

understanding of tectonic setting and processes that were operative during the metamorphic event (England and Thompson, 1984; Thompson and England, 1984; Bohlen, 1987, 1991; Essene, 1989; Harley, 1989; Brown, 1993; Vernon, 1996). Determination of P–T paths of metamorphism is of particular importance in this regard because variations of pressure and temperature that characterize a metamorphic event are considered to be a function of the tectonic setting and of the heat-generating processes (England and Thompson, 1984; Thompson and England, 1984; Mezger, Bohlen, and Hanson, 1990; Sharp and Essene, 1991; Harley, 1989; Brown, 1993; Vernon, 1996). Generally, clockwise, especially isothermal decompressional, P–T–t paths are considered to develop in continent-continent collisional environments (England and Thompson, 1984; Thompson and England, 1984; Harley, 1989; Brown, 1993), whereas anticlockwise, especially isobaric cooling, P–T–t paths are related to the intrusion and underplating of mantle magma which can occur in continental magmatic arc regions (Wells, 1980; Bohlen, 1987, 1991), hot spots related to mantle plumes (Hill and others, 1992; Zhao and others, 1998, 1999), and rift environments (Sandiford and Powell, 1986). Thus, investigations on the tectonothermal evolution of metamorphism can elucidate the tectonic setting and evolution of the South China craton.

In this paper, we present metamorphic and structural data for the Mesoproterozoic Mayuan assemblage which lies along the northern margin of the Cathaysia Block. We examine metamorphic textures and mineral assemblages to establish the evolutionary stages of metamorphism, use phase diagram analysis and P–T grid to study the sequence

of mineral assemblages and reaction history; and apply the TWEEQU technique and conventional thermobarometry to estimate metamorphic P–T conditions and define the P–T path, which in combination with structural and geochronological data place important constraints on the tectonic model of the evolution of the Cathaysia and Yangtze blocks in the Neoproterozoic.

REGIONAL SETTING

The Yangtze Block.–The Yangtze Block of the South China craton consists of a Paleoproterozoic to Mesoproterozoic metamorphic basement overlain by a Neoproterozoic (Sinian) to Cenozoic cover. The basement is divided into three lithotectonic assemblages: Kangding, Sibao, and Banxi. The Kangding assemblage is only exposed along the southwestern and northwestern margins of the Yangtze Block and consists of supracrustal rock and granitic gneiss metamorphosed to amphibolite, and locally to granulite, facies. The supracrustal rocks include paragneiss, mica schist, graphite-bearing sillimanite–garnet pelitic gneiss (khondalite), amphibolite, marble, and quartzite. The available geochronological data determined by a variety of techniques and of varying reliability indicate that the assemblage formed at 2500 to 2000 Ma and underwent metamorphism and deformation at 2000 to 1900 Ma (Yuan, 1985; Li and others, 1987; Wu, 1988; Yao and Wei, 1994).

The Sibao assemblage crops out over the whole block and is composed of an arenaceous to argillaceous sedimentary package, with minor volcanic and tuffaceous rocks. The available Sm–Nd and U–Pb ages of these rocks range from 1772 to 1332 Ma (Li and Leng, 1987; Han, 1994; Yao and Wei, 1994); suggesting that they formed between the Paleoproterozoic and Mesoproterozoic. The syn-tectonic granites yielded Rb–Sr ages of 1063 ± 95 and 957 ± 64 Ma (Wu, 1979) and a zircon U–Pb age of 1145 ± 40 (Yie, 1990), whereas a post-tectonic granite yielded a SHRIMP zircon U–Pb age of 819 ± 9 Ma (Li, 1999). These isotopic data suggest the Sibao assemblage underwent regional metamorphism at the end of Mesoproterozoic (Wang and Qiao, 1984; Wang and Mo, 1995).

The Banxi assemblage unconformably overlies the Sibao assemblage and itself formed the basement upon which the younger Sinian to post-Sinian covering rocks were deposited. The assemblage crops out in a northeast trending belt along the southeast margin of the Yangtze block and is lithologically similar to the Sibao assemblage, dominated by flysch and slates but with a proportion of igneous rocks, represented by ophiolite and glaucophane-jadeite schist (Yang, 1988; Yao and Wei, 1994; Zhang, 1994). Available isotopic data constrain the protolithic age of the Banxi assemblage to between 1100 to 900 Ma and the metamorphic crystallization and cooling ages to between 870 to 820 Ma (Chen and others, 1991; Xu, 1992; Gan and others, 1993; Ma and Wang, 1994).

The Cathaysia Block.–The Cathaysia Block is divided into four unconformity- or fault-bounded lithotectonic units: Badu, Mayuan, Wuyi–Yunkai, and Pingtan–Dongshan (fig. 2; Zhao, Sun, and He, 1994a). The Badu assemblage constitutes the oldest basement unit recognized in the block and consists of graphite-bearing pelitic gneiss and schist, felsic gneiss, magnetite quartzite, amphibolite, calcsilicate rock, and marble, along with minor pre- and syn-tectonic plutons. Amphibolites from the Badu assemblage yielded Sm–Nd whole-rock isochron ages of 2199 ± 52 and 2059 ± 52 Ma, and felsic gneisses yielded zircon U–Pb ages of 2032 ± 16 and 2004 ± 10 Ma (Hu, 1991). These data are interpreted as their protolithic ages (Hu, 1991). The rocks from the Badu assemblage underwent widespread upper amphibolite facies metamorphism, anatexis, and polyphase deformation (Zhao, Sun, and He, 1994b) at approx 1800 Ma, which is constrained by a zircon U–Pb age of 1837 ± 52 Ma from syn-tectonic granites and a Rb–Sr whole-rock isochron age of 1813 ± 9 Ma from paragneisses (Shui, 1987; Xu and Shui, 1988; Hu, 1991).

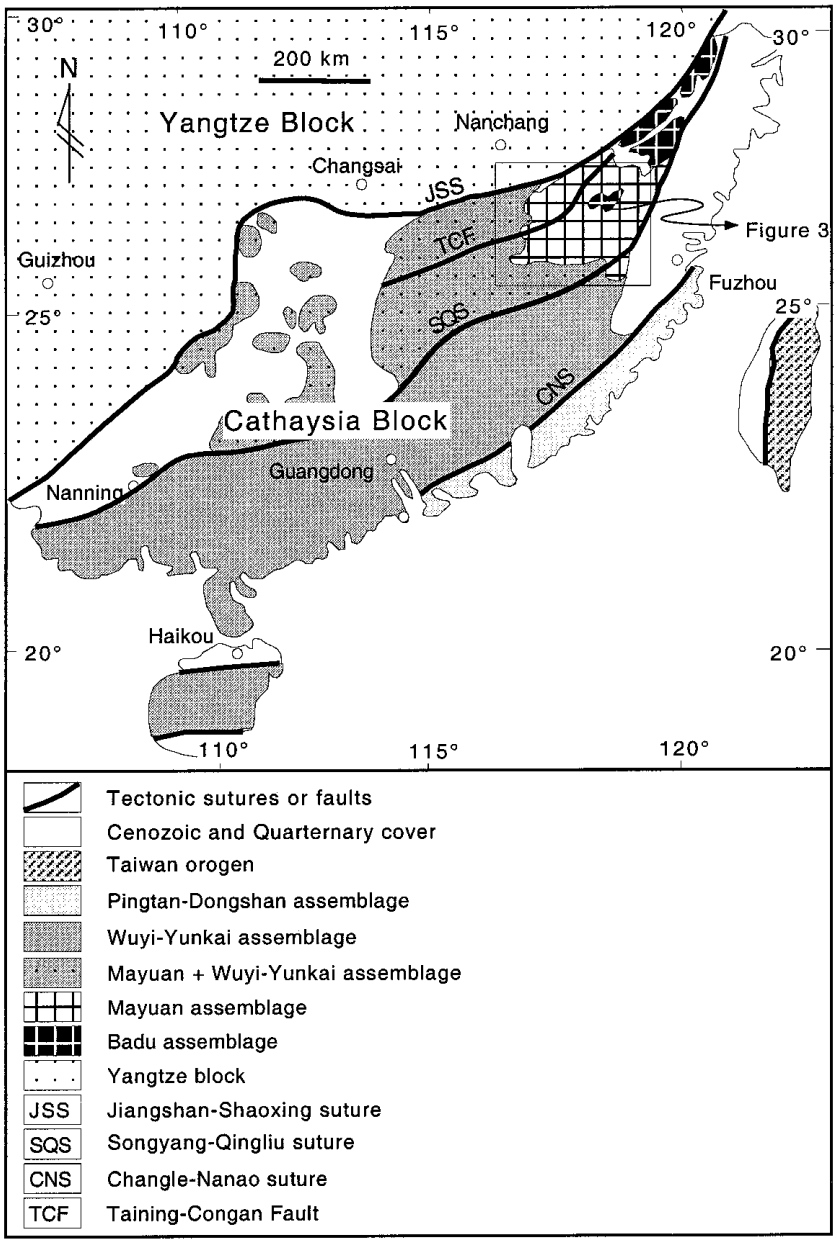

Fig. 2. Geological sketch map of the Cathaysia Block showing the spatial distribution of the major tectonic assemblages and sutures (faults).

The Mayuan assemblage consists of felsic paragneiss, pelitic schist, greenschist, amphibolite, marble, calcsilicate, quartzite, and meta-keratophyre. Meta-keratophyres were dated using the conventional zircon U–Pb methods at 1438 ± 41 and 1100 ± 9 Ma, and amphibolites were dated using the Sm–Nd whole-rock isochron methods at 1376 ± 82 Ma. These ages are interpreted as their protolithic ages. The assemblage underwent

polyphase deformation and metamorphism at around 850 Ma, defined by a hornblende K–Ar age of 844 Ma from amphibolites and U–Pb ages of 890 to 860 Ma from syn-tectonic migmatites and granites (Shui, 1987; Xu and Shui, 1988; Li, 1988, 1989; Gan and others, 1993).

The Wuyi–Yunkai assemblage consists of graywacke, siltstone, and quartzite, with minor tuffaceous rock. The unit underwent sub-greenschist facies metamorphism and a single phase of deformation. The available isotopic data indicate that these rocks formed between the Neoproterozoic and Early Paleozoic and underwent regional metamorphism in the Early Paleozoic at approx 440 to 415 Ma (Li, 1988, 1989; Yang, 1988; He and Zhang, 1989; Gao, 1991).

The Pingtan–Dongshan assemblage outcrops along the southeastern margin of the Cathaysia Block (fig. 2) and consists of sandstone, siltstone, argillite, quartzite, and carbonate (Chen, 1997). Paleontological and geochronological data, along with regional correlations indicate a Paleozoic and Early Mesozoic age for the rocks with very low grade metamorphism and a single phase of deformation at approx 170 Ma (Huang, 1989; Gao, 1991; Chen, 1997).

The Jiangshan–Shaoxing Fault.–The 2000 km long northeast–southwest trending Jiangshan–Shaoxing Fault is a major tectonic boundary separating the Yangtze and Cathaysia blocks (fig. 1). With discovery of large amounts of ophiolites and blueschists along the fault, it has been interpreted as a collisional suture which welded the blocks (Shui, 1987; Hsü and others, 1988, 1990; Jahn, Zhou, and Li, 1990; Chen and others, 1991; Xu, 1992). The ophiolites yielded a Sm–Nd age of 1034 $\pm$ 24 Ma, interpreted as the protolithic age and predating the timing of suturing (Chen and others, 1991). Glaucophanes from blueschists along the suture were dated using the K–Ar methods at 866 $\pm$ 14 Ma, interpreted as the age of the peak metamorphism or the timing of suturing (Ma and Wang, 1994), and gastalites from the same blueschists yielded the K–Ar age of 799 $\pm$ 9.2 Ma, which may represent the cooling age of the suture zone.

Although the Jiangshao–Shaoxing Fuault constitutes the Neoproterozoic collisional boundary between the Yangtze and Cathaysia blocks, it shows evidence for a long and complex history of movement. The fault also disrupts the Neoproterozoic and post-Neoproterozoic unmetamorphosed strata in the Cathaysia Block, suggesting that final movement on the fault postdates assembly of the South China craton. This late movement possibly accounts for the offset in the highest grade metamorphic rocks in the Mayuan assemblage from the suture boundary (fig. 3).

STRUCTURAL GEOLOGY

Overprinting relationships allow the recognition of three main deformation events (D_1, D_2, and D_3) in the area. The regional structure of the Mayuan assemblage is characterized by large-scale antiform-synform pairs (figs. 3 and 4) in which the higher grade metamorphic rocks occupy the antiformal hinge zones (Jianyang–Pucheng region; fig. 3), whereas lower grade rocks occur in synforms (Hu, 1984; Zhu, 1985; Zhao, Sun, and He, 1994a). Structural analysis reveals these composite structures developed during three deformational episodes (D_1-D_3), but were mainly shaped by the last episode of deformation (D_3), which resulted in the folding of the metamorphic isograds developed during D_2 (Hu, 1984; Zhu, 1985; Zhao, Sun, and He, 1994a). D_3 has also resulted in the folding or crenulation of the regional foliation (S_2) and the development of a weak spaced cleavage (S_3), and a mineral lineation (L_3) defined by sillimanite and hornblende (Zhu, 1985; Zhao, Sun, and He, 1994a).

The D_1 deformational fabrics are poorly preserved due to overprinting and transposition by subsequent deformational events. Evidence for this event includes small rootless intrafolial folds (F_1) and an associated early foliation (S_1) within garnet, staurolite, and biotite porphyroblasts in pelitic schist. D_2 is characterized by ubiquitous isoclinal

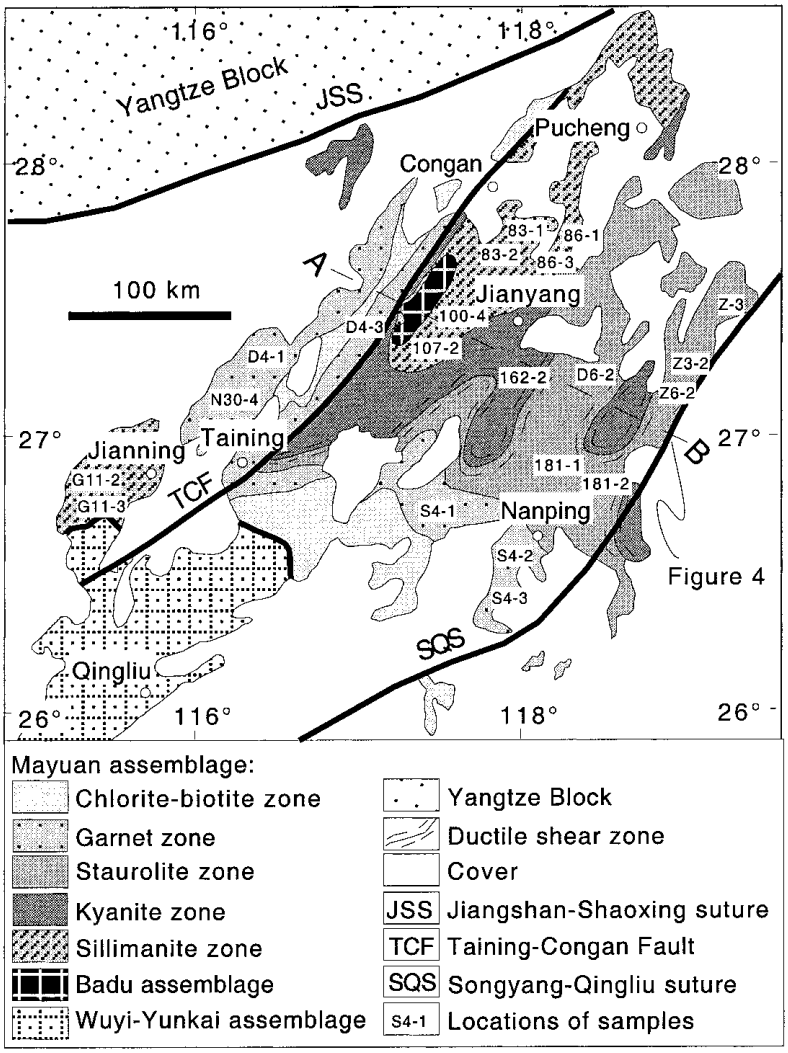

Fig. 3. Metamorphic isograd map of the Mayuan assemblage.

folds on various scales and a penetrative foliation (S_2), along with boudin and mullion lineation structures (L_2). Also associated with D_2 are a series of regional-scale ductile shear zones with a mylonitic foliation parallel to the regional foliation (S_2). D_3 antiform-synform pairs trend northeast-southwest. The main D_3 antiform lies in the footwall to, and is truncated by, the Taining-Congan Fault (fig. 4). The highest grade rocks are exposed in the core of this structure and envelope an inlier of the Badu assemblage (fig. 3). Final movement on the fault is post-D3. Kinematic data for the Taining–Congan Fault are not preserved, but relations across it are consistent with a normal sense of movement.

METAMORPHIC ZONES OF THE MAYUAN ASSEMBLAGE

On the basis of mineral assemblages in pelitic schist, the Mayuan assemblage can be divided into a Barrovian-type facies series of chlorite–biotite, garnet, staurolite, kyanite, and sillimanite zones (fig. 3). Boundaries between zones are marked by the first

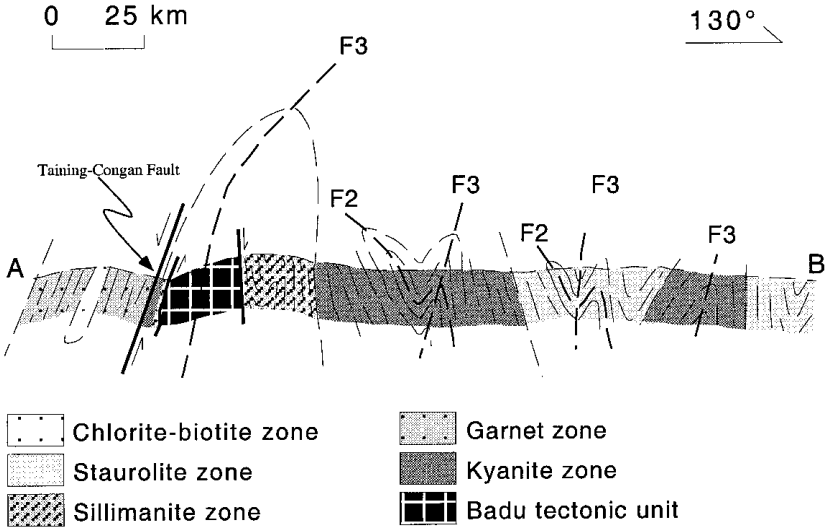

Fig. 4. Schematic cross section of the Mayuan assemblage.

appearance of the diagnostic metamorphic minerals in pelitic schist (Zhao, Sun, and He, 1994b, 1996), except for the kyanite zone which is separated from the staurolite zone by ductile shear zones (fig. 3; Hu, 1984; Zhu, 1985; Zhao, Sun, and He, 1994a). East of the Taining–Congan Fault there is an overall increase in metamorphic grade from the south to north. West of the fault, the zones are distributed about a synform (fig. 3). Within the sillimanite zone there is a fault-bounded inlier of the Badu assemblage which consists of Paleoproterozoic felsic gneisses (Li, 1988).

Chlorite–biotite zone.–This zone mainly outcrops in the southern and western parts of the area and constitutes the lowest grade rocks of the Mayuan assemblage (fig. 3). It contains fine-grained biotite porphyroblast-bearing chlorite-muscovite (sericite) schist, biotite-plagioclase paragneiss, chlorite schist (greenschist), metacarbonate, and quartzite. Accessory minerals within the pelitic schist and felsic paragneiss include pyrite, pyrrhotite, apatite, tourmaline, and graphite.

Garnet zone.–East of the Taining–Congan Fault, the first occurrence of garnet is immediately north of the chlorite–biotite zone in chlorite-mica schist. Garnet-bearing rocks are also widely distributed along the western side of the fault (fig. 3). The garnet mica schist that characterizes this zone is interbanded with fine- and medium-grained biotite gneiss, actinolite–chlorite–epidote–albite mafic schist (greenschist), marble, and quartzite. The modal abundance of chlorite in mica schist in this zone is less than that in the chlorite–biotite zone, and is inferred to have been consumed in biotite and garnet generating reactions. Accessary mineral phases are similar to those in the chlorite–biotite zone.

Staurolite zone.–The staurolite zone is widespread to the east of the Taining–Congan Fault. Staurolite occurs sporadically as coarse-grained porphyroblasts in biotite schist throughout the zone. Associated lithologies include fine- to medium-grained garnet-bearing or garnet-free felsic paragneiss, actinolite–epidote–albite mafic schist (greenschist), tremolite–quartz marble, and quartzite. Compared to the garnet zone, chlorite is a rare phase, and biotite is more abundant. Coarse-grained tourmaline occurs in association with garnet and staurolite in this zone.

Kyanite zone.–In addition to kyanite-bearing pelitic schist, the rocks in this zone also include medium-grained felsic paragneiss, phlogopite-tremolite marble, and quartzite.

Within the zone, staurolite and garnet coexist with kyanite, biotite is widespread, and chlorite and muscovite are only present in very minor amounts.

Sillimanite zone.–The sillimanite zone is exposed in the northern and southern parts of the area along the eastern and western sides respectively, of the Taining–Congan Fault (fig. 3). Sillimanite–mica schist occurs in association with medium- to coarse-grained epidote amphibolite, tremolite–phlogopite marble, and quartzite. Within the zone, chlorite, garnet, and staurolite are absent in sillimanite-bearing rocks, and kyanite is rare and occurs as relict crystals. Muscovite is generally a very minor matrix phase, but clusters of coarse-grained, randomly-oriented muscovite are commonly observed, associated with sillimanite in mica schist from this zone.

METAMORPHIC STAGES

Based on microstructural relations between mineral phases and deformational episodes in the Mayuan assemblage, four separate metamorphic stages (M_1-M_4) have been interpreted (fig. 5). M_1 is represented by mineral inclusions within porphyroblasts and is preserved within all zones in the area. In pelitic schist, the most complete mineral assemblage identified for the M_1 stage consists of chlorite + muscovite + biotite + plagioclase + quartz ± garnet (core), preserved within coarse-grained biotite, garnet, and staurolite porphyroblasts. In mafic rocks, the typical M_1 mineral assemblage is actinolite + chlorite + epidote + albite + quartz, enclosed in coarse-grained amphibole and plagioclase. In most cases, the M_1 minerals are oriented, defining the internal

Deformation	D_1	D_2	D_3	
Metamorphism	M_1	M_2	M_3	M_4
Pelitic schists	Pl (i) Qtz (i) Chl (i) Bt (i) Mu (i) Gr (i) Grt (p-c)	Grt (p-r) St (p) Ky (p) Pl (m) Qtz (m) Bt (p+m) Mu (m) Gr (m)	Sil (p-r) Bt (p) Mu (p) Qtz (m) Pl (m-r)	Chl (re) Ms (re) Grt (r)
Mafic rocks	Ab (i) Qtz (i) Chl (i) Act (i) Ep (i)	Ab (m) Qtz (m) Tr (p+m) Chl (m) Ep (m)	Hbl (p-r) Pl (p) Qtz (m)	Chl (re) Act (re) Ep (re)
Metacarbonates	Cc (i) Qtz (i) Phl (i)	Cc (m) Qtz (m) Tr (p) Phl (m) Pl (m)	Cc (re) Zo (re)	

Fig. 5. Metamorphic mineral crystallization–deformation diagram for the pelitic schists, amphibolites and metacarbonates in the Mayuan assemblage. Symbols are: i, inclusion; m, matrix; m-r, the rim of matrix; p, porphyroblast; p-c, the core of porphyroblast; p-r, the rim of porphyroblast; p + m, porphyroblast + matrix; r, rim; re, retrogressive minerals. Mineral symbols are after Kretz (1983).

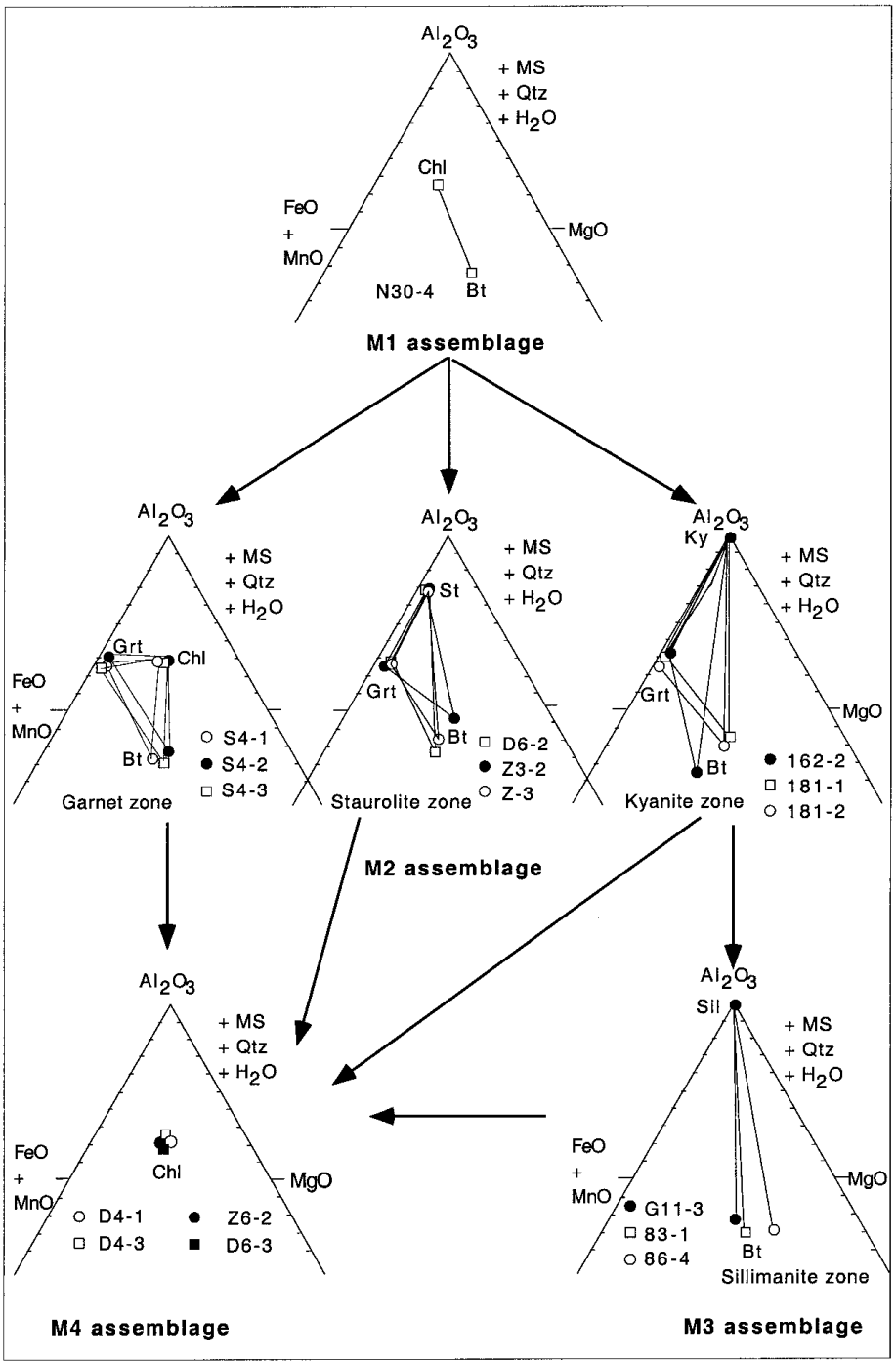

Fig. 6. Al_2O_3–(FeO + MnO)–MgO (AFM) projection of the M1, M2, M3 and M4 mineral assemblages in the Mayuan metapelites. Mineral symbols are after Kretz (1983).

schistosity (S_1) within the porphyroblast. S_1 is oblique to the external matrix foliation (S_2), suggesting that M_1 developed earlier than the second phase of deformation (D_2).

M_2 represents formation of coarse-grained biotite, garnet (rim), staurolite, kyanite, and amphibole porphyroblasts and resulted in the development of chlorite-biotite, garnet, staurolite, and kyanite zones. The characteristic mineral assemblages for pelitic, mafic, and carbonate rocks from the chlorite-biotite, garnet, staurolite, and kyanite zones are shown in figure 5. In pelitic schists, no reaction relations between garnet, staurolite, and kyanite were observed, and as metamorphic grade increases from chlorite-biotite to kyanite zones, the abundance of chlorite and muscovite decreases, at the expense of biotite, garnet, staurolite, and kyanite. The chlorite, muscovite, and biotite of M_2 are strongly oriented and define the regional schistosity (S_2). In addition, garnet and staurolite porphyroblasts show "snowball structures," indicating that the M_2 stage coincides with the D_2 phase of deformation.

M_3 is restricted to, and is characteristic of, the sillimanite zone and is represented by the formation of a sillimanite + quartz + biotite + muscovite + plagioclase assemblage in pelite and a hornblende + plagioclase assemblage in amphibolite. Amphibolites occur as thin layers (0.5-5 m thick) interbedded with sillimanite mica schists. In the same outcrop, sillimanite in pelitic schist and hornblende in amphibolite show the same preferred orientation and define the D_3 mineral lineation (L_3). This suggests that the M_3 stage was synchronous with the D_3 phase of deformation.

The last metamorphic stage M_4 resulted in retrograde assemblages of muscovite (sericite) + epidote + chlorite, replacing garnet, staurolite, kyanite, and sillimanite in pelite and actinolite + epidote + chlorite + albite, replacing hornblende and plagioclase in amphibolite. These retrogressive minerals do not show a preferred orientation, suggesting that they formed after the final deformational episode (post-D_3).

MINERAL COMPOSITIONS

Mineral compositions were analyzed using an EPM–810Q electron microprobe. Analyses were performed with an accelerating voltage of ~15 kV, a beam current of 17 to 20 nA, and a spot size of 2 to 10 μm. Natural minerals were used as standards for major elements with synthetic oxides and silicate minerals used for some minor elements. Sixteen pelitic schist and five amphibolite samples were chosen as the most appropriate for characterizing the different stages of tectonothermal evolution, and their locations are given in figure 3. A representative selection of mineral compositions is included in tables 1 to 6.

Garnet.–Garnet compositions (table 1) were determined from the cores of large porphyroblast grains containing the inclusion mineral assemblage (M_1), from inclusion-free rims surrounded by matrix plagioclase or quartz grains from different metamorphic zones (M_2), and from rims surrounded by retrogressive chlorite and muscovite (M_4). All garnet crystals are essentially almandine, with appreciable amounts of spessartine, grossular, pyrope, and andradite components. Garnet from the garnet and staurolite zones shows a core to rim increase in pyrope content, which we interpret as having developed during the prograde growth of the garnet. A systematic compositional difference occurs between garnet-zone and staurolite-zone garnet with the latter showing an increase in pyrope, almandine, and andradite and a decrease in grossular and spessartine. These variations do not extend to the kyanite zone, in which garnet shows higher grossular and lower spessartine and pyrope contents than the garnet from the garnet and staurolite zones. The rim compositions of garnet surrounded by retrogressive chlorite and muscovite (M_4) differ from those of garnet surrounded by matrix plagioclase and quartz grains with the former having higher almandine and lower spessartine contents than the latter.

TABLE 1

Garnet compositions of mica schists from the Mayuan assemblage

Sample	N30-4	S4-1	S4-3	Z3-2	162-2	181-2	S4-1	S4-2	S4-3	D6-2	Z3-2	Z-3	162-2	181-1	181-2	D4-1	D4-3	Z6-2	D6-2
Zones	Grt	Grt	Grt	St	Ky	Ky	Grt	Grt	Grt	St	St	St	Ky	Ky	Ky	Grt	Grt	St	St
Textures	C	C	C	C	C	C	R1	R1	R1	R1	R1	R1	R1	R1	R1	R2	R2	R2	R2
SiO_2	34.85	38.63	37.47	37.69	36.07	34.81	37.46	38.02	37.24	35.09	35.60	34.41	35.67	36.63	35.62	37.22	37.52	35.65	37.49
Al_2O_3	20.16	19.99	19.67	19.80	19.48	20.25	20.12	20.02	22.64	20.57	20.95	20.42	20.43	20.25	20.65	20.45	20.04	20.22	20.95
FeO*	32.37	25.11	25.65	24.49	30.34	31.29	28.54	24.82	23.55	32.49	37.79	35.86	30.89	28.22	28.38	36.49	37.60	38.00	36.12
MnO	6.38	7.39	7.43	8.75	6.36	5.26	7.61	12.62	11.26	8.97	2.64	4.11	3.35	5.53	4.96	2.31	2.66	3.38	2.64
MgO	1.64	0.67	0.86	0.61	1.34	1.16	1.88	1.67	1.48	2.23	2.01	2.51	1.25	1.31	1.12	1.28	1.68	1.24	1.01
CaO	5.57	8.28	8.14	8.19	5.20	6.49	3.52	2.86	4.75	1.60	2.09	1.51	8.47	8.60	8.23	2.54	1.51	2.57	2.09
Totals	100.97	100.07	99.23	99.53	98.79	99.26	99.13	100.01	100.92	100.95	101.08	98.82	100.06	100.54	98.97	100.29	101.00	101.06	100.30
Si	2.817	3.094	3.045	3.053	2.965	2.853	3.048	3.071	2.955	2.843	2.869	2.838	2.880	2.935	2.901	3.023	3.031	2.892	3.035
Al	1.921	1.888	1.884	1.891	1.888	1.956	1.930	1.906	2.118	1.965	1.990	1.986	1.944	1.913	1.983	1.958	1.909	1.934	1.999
Fe^{3+}	0.451	0.000	0.028	0.001	0.171	0.346	0.000	0.000	0.000	0.356	0.277	0.348	0.297	0.214	0.205	0.000	0.031	0.288	0.000
Fe^{2+}	1.688	1.682	1.713	1.658	1.896	1.760	1.942	1.676	1.563	1.807	2.257	2.087	1.755	1.653	1.705	2.478	2.505	2.276	2.445
Mn	0.437	0.501	0.511	0.600	0.443	0.365	0.525	0.863	0.757	0.616	0.180	0.287	0.229	0.375	0.342	0.159	0.182	0.232	0.181
Mg	0.198	0.080	0.104	0.074	0.164	0.142	0.228	0.201	0.175	0.269	0.241	0.309	0.150	0.156	0.136	0.155	0.202	0.150	0.122
Ca	0.482	0.711	0.709	0.711	0.458	0.570	0.307	0.247	0.404	0.139	0.180	0.133	0.733	0.738	0.718	0.221	0.131	0.219	0.181
Adr	0.226	0.000	0.014	0.001	0.086	0.173	0.000	0.000	0.000	0.178	0.138	0.174	0.148	0.107	0.102	0.000	0.016	0.144	0.000
Prp	0.071	0.027	0.034	0.024	0.055	0.050	0.076	0.067	0.060	0.095	0.084	0.109	0.052	0.053	0.047	0.051	0.067	0.052	0.042
Sps	0.156	0.168	0.168	0.197	0.150	0.129	0.175	0.289	0.261	0.218	0.063	0.102	0.080	0.128	0.118	0.053	0.060	0.081	0.062
Alm	0.602	0.566	0.564	0.545	0.640	0.620	0.647	0.561	0.539	0.638	0.790	0.741	0.612	0.566	0.588	0.822	0.829	0.791	0.834
Grs	0.069	0.239	0.220	0.233	0.068	0.018	0.102	0.083	0.139	0.000	0.000	0.000	0.100	0.143	0.142	0.073	0.028	0.000	0.062

C, core in contact with inclusions; R1, rim in contact with matrix plagioclase or quartz grains; R2, rim in contact with retrogressive chlorite and muscovite grains. Adr = $Fe^{3+}/2$; Prp = $Mg/(Fe^{2+} + Mg + Mn + Ca)$; Sps = $Mn/(Fe^{2+} + Mg + Mn + Ca)$; Alm = $Fe^{2+}/(Fe^{2+} + Mg + Mn + Ca)$; Grs = $Ca/(Fe^{2+} + Mg + Mn + Ca)$. Fe^{3+} is derived following the scheme of Droop (1987). Minerals symbols are after Kretz (1983).

Plagioclase.–Analyzed plagioclase grains (table 2) include (1) inclusion-type plagioclase enclosed in garnet and staurolite porphyroblasts in pelite (M_1); (2) matrix-type plagioclase from the garnet, staurolite, and kyanite zones in pelite (M_2); and (3) plagioclase from amphibolite associated with sillimanite-bearing schist in the sillimanite zone (M_3). A clear compositional difference exists between the inclusion-type and matrix-type plagioclase. The inclusion-type plagioclase is andesine with $An_{30–35}$, whereas the matrix-type plagioclase is oligoclase with $An_{13–25}$ (table 2). Matrix-type plagioclase shows a decrease in anorthite content from the garnet zone (An_{20-30}) through the staurolite zone (An_{13-25}) to the kyanite zone (An_{14-15}). Plagioclase from amphibolite is andesine (An_{40-45}).

Biotite and muscovite.–Tables 3 and 4 list the representative compositions of inclusion-type biotite and muscovite surrounded by plagioclase and quartz and enclosed in garnet and staurolite porphyroblasts, and matrix-type biotite and muscovite from the garnet, staurolite, and kyanite zones in pelitic schist. Inclusion-type biotite generally has a higher X_{Mg} ($X_{Mg} = Mg/(Mg + Fe)$) value than matrix-type biotite. The matrix-type biotite from the kyanite and sillimanite zones shows a slightly higher X_{Mg} value than that from the garnet and staurolite zones. There is no distinct compositional variation between the inclusion-type and matrix-type muscovite or between muscovite from the different metamorphic zones. All are phengitic, with both celadonite and paragonite contents of less than 20 mole percent.

Chlorite, staurolite, and hornblende.–Two textural types of chlorite were analyzed, the first defining the S_2 foliation in the matrix and grown during M_2, and the second replacing garnet and staurolite porphyroblasts during the M_4 stage (table 5). The former type of chlorite is clinochlore, whereas the latter is penninite with the retrogressive chlorite containing higher Al_2O_3 and FeO, but lower SiO_2 and MgO than the matrix chlorite. This results in higher X_{Mg} and Al^{IV} but lower Si and Mg in the retrogressive chlorite. Typical compositions of staurolite in the staurolite and kyanite zones are shown in table 5. There is no pronounced difference in chemical composition between staurolites from the two zones, except that staurolite in the kyanite zone has higher Al_2O_3 contents than that in the staurolite zone (table 5). Hornblende in amphibolite associated with sillimanite-bearing schist is tschermakitic Ca-amphibole, with Al^{IV} around 1.660 to 1.715 and Na^A between 0.449 to 0.598 (table 6).

PHASE RELATIONS AND REACTION HISTORY

The observed mineral assemblages, their textural relations and their chemical compositions can be used to decipher the reaction history of the studied rocks. Because the Mayuan pelitic schists invariably contain muscovite and quartz, we will use the AFM projection (Thompson, 1957) to illustrate phase compatibilities. A H_2O-dominant hydrous fluid (vapor) phase is assumed to be in excess. MnO is an essential component for garnet, and, thus, is taken into account in the AFM diagrams (Symmes and Ferry, 1992). The representative AFM projections for different mineral assemblages recognized in the Mayuan pelitic schists are shown in figure 6.

Chlorite-biotite zone.–The co-occurrence of biotite + chlorite within this zone is probably related to the following chlorite- and muscovite-consuming dehydration reaction:

$$\text{(Fe–Mg) chlorite} + \text{muscovite} = \text{biotite} + \text{Al-rich chlorite} + \text{quartz} + H_2O \quad (1)$$

Because of the lack of clear textural relations, however, metamorphic reactions responsible for the transition from M_1 to M_2 assemblages in the chlorite-biotite zone cannot be established accurately.

Garnet-in reactions.–The AFM topologies seen in the M_1 assemblage and garnet zone (fig. 6) suggest that biotite from the M_1 assemblage may not have been involved in the

TABLE 2

Plagioclase compositions of mica schists and amphibolites from the Mayuan assemblage

Sample	N30-4	S4-1	S4-3	Z3-2	162-2	181-2	S4-1	S4-2	S4-3	D6-2	Z3-2	Z-3	162-2	181-1	181-2	G11-2	83-2	86-3	100-4	107-2
Rocks	Pelitic schists															Amphibolites				
Zones	Grt	Grt	Grt	St	Ky	Ky	Grt	Grt	Grt	St	St	St	Ky	Ky	Ky	Sil	Sil	Sil	Sil	Sil
Textures	I	I	I	I	I	I	M	M	M	M	M	M	M	M	M	M	M	M	M	M
SiO_2	62.28	62.33	62.46	61.32	62.22	61.43	63.49	61.49	58.34	62.29	63.44	62.78	63.35	63.34	63.52	57.93	58.04	56.39	57.65	58.03
Al_2O_3	22.91	26.43	26.39	25.44	22.58	21.99	24.46	26.36	26.98	25.41	25.36	22.48	21.53	24.48	24.17	25.48	26.03	25.87	25.96	25.01
FeO*	0.04	0.00	0.00	0.00	0.04	0.17	0.00	0.13	0.40	0.01	0.02	0.08	0.04	0.27	0.14	0.18	0.09	0.10	0.01	0.00
MgO	0.03	0.00	0.03	0.00	0.03	0.02	0.01	0.02	0.21	0.03	0.03	0.03	0.03	0.03	0.03	0.02	0.00	0.03	0.02	0.00
CaO	6.63	5.74	5.91	6.27	6.78	6.37	5.10	3.80	6.08	2.54	4.32	4.53	3.42	3.09	2.87	9.17	9.17	9.74	8.92	9.32
Na_2O	7.80	6.51	6.12	8.29	7.97	8.52	8.17	8.50	7.38	9.02	6.91	9.84	10.93	9.61	8.74	6.07	6.02	6.18	6.67	6.24
K_2O	0.06	0.22	0.10	0.00	0.04	0.07	0.04	0.13	0.12	0.04	0.06	0.06	0.04	0.16	0.04	0.49	0.62	0.52	0.48	0.61
Totals	99.75	101.23	101.01	101.33	99.66	98.57	101.27	100.43	99.51	99.34	100.14	99.80	99.34	100.98	99.51	99.34	99.97	98.83	99.71	99.21
Si	2.770	2.710	2.716	2.690	2.773	2.774	2.766	2.700	2.607	2.752	2.771	2.792	2.829	2.768	2.798	2.611	2.604	2.570	2.593	2.627
Al	1.201	1.355	1.353	1.315	1.187	1.171	1.256	1.365	1.422	1.324	1.306	1.179	1.133	1.261	1.255	1.354	1.377	1.390	1.377	1.335
Fe	0.001	0.000	0.000	0.000	0.001	0.006	0.000	0.004	0.013	0.000	0.001	0.003	0.001	0.009	0.005	0.006	0.003	0.003	0.000	0.000
Mg	0.002	0.000	0.002	0.000	0.002	0.001	0.001	0.001	0.014	0.002	0.002	0.002	0.002	0.002	0.002	0.001	0.000	0.002	0.001	0.000
Ca	0.316	0.267	0.275	0.295	0.324	0.308	0.238	0.179	0.291	0.120	0.202	0.216	0.164	0.145	0.135	0.443	0.441	0.476	0.430	0.452
Na	0.673	0.549	0.516	0.706	0.689	0.746	0.690	0.724	0.640	0.773	0.585	0.849	0.946	0.814	0.746	0.530	0.524	0.546	0.582	0.548
K	0.003	0.012	0.006	0.000	0.002	0.004	0.002	0.007	0.007	0.002	0.003	0.003	0.002	0.009	0.002	0.028	0.036	0.030	0.028	0.035
Sum	4.967	4.893	4.868	5.006	4.978	5.011	4.953	4.981	4.996	4.973	4.870	5.043	5.078	5.009	4.945	4.975	4.985	5.019	5.011	4.997
An	31.9	32.2	34.5	29.5	31.9	29.1	25.6	19.7	31.0	13.4	25.6	20.2	14.7	15.0	15.3	44.3	44.0	45.2	41.3	43.7
Ab	67.8	66.3	64.7	70.5	67.9	70.5	74.2	79.6	68.2	86.4	74.1	79.5	85.1	84.0	84.5	52.9	52.3	51.9	55.9	52.9
Or	0.3	1.5	0.8	0.0	0.2	0.4	0.2	0.7	0.8	0.2	0.3	0.3	0.2	1.0	0.2	2.8	3.7	3.9	3.8	4.4

I, inclusions; M, matrix. An = Ca/(Ca + Na + K); Na = Na/(Ca + Na + K); Or = K/(Ca + Na + K). Mineral symbols are after Kretz (1983).

TABLE 3

Biotite compositions of mica schists from the Mayuan assemblage

Sample	N30-4	S4-1	S4-3	Z3-2	162-2	81-2	S4-1	S4-2	S4-3	D6-2	Z3-2	Z-3	162-2	181-1	181-2	G11-3	83-1	86-4
Textures	inclusions						matrix											
Zones	Grt	Grt	Grt	St	Ky	Ky	Grt	Grt	Grt	St	St	St	Ky	Ky	Ky	Sil	Sil	Sil
SiO_2	37.93	33.77	34.26	33.77	36.44	33.62	35.63	35.64	34.99	32.87	39.45	37.09	34.01	35.88	33.63	33.97	35.35	36.13
TiO_2	1.41	1.39	1.37	1.39	1.40	1.25	1.63	1.86	1.66	1.79	1.11	1.34	1.57	1.63	1.42	2.53	2.20	2.54
Al_2O_3	17.01	20.79	19.96	20.79	20.89	20.84	19.26	20.16	20.75	17.45	22.57	19.73	18.38	20.34	20.93	20.42	19.25	18.09
FeO*	15.61	21.85	17.04	20.84	16.31	18.36	20.11	18.45	17.60	23.71	15.60	19.83	21.18	19.35	20.48	18.60	15.33	17.42
MnO	0.10	0.04	0.44	0.04	0.12	0.02	0.18	0.34	0.34	0.28	0.04	0.08	0.06	0.04	0.04	0.44	0.26	0.16
MgO	12.61	10.27	11.04	10.27	12.73	12.37	9.11	9.34	9.67	9.25	9.47	9.36	6.53	10.20	10.66	10.55	13.82	11.75
Na_2O	0.47	0.39	0.10	0.39	0.41	0.23	0.06	0.14	0.13	0.26	0.22	0.03	0.19	0.29	0.14	0.20	0.17	0.22
K_2O	8.34	8.26	9.27	7.26	8.30	8.51	9.39	9.60	9.37	8.39	7.54	8.26	9.16	8.35	9.13	9.29	9.13	9.37
Totals	93.49	96.77	93.48	94.75	96.61	95.21	95.38	95.54	94.52	94.23	93.57	95.73	94.74	96.55	95.03	96.00	95.52	95.69
Si	2.862	2.532	2.632	2.559	2.651	2.527	2.715	2.692	2.660	2.579	2.836	2.776	2.620	2.660	2.573	2.561	2.619	2.713
Ti	0.080	0.078	0.079	0.079	0.077	0.071	0.093	0.106	0.095	0.106	0.060	0.075	0.091	0.091	0.082	0.143	0.123	0.143
Al^{IV}	1.138	1.468	1.368	1.441	1.349	1.473	1.285	1.308	1.340	1.421	1.164	1.224	1.380	1.340	1.427	1.439	1.381	1.287
Al^{VI}	0.375	0.370	0.440	0.416	0.234	0.374	0.445	0.387	0.520	0.193	0.749	0.517	0.289	0.338	0.461	0.376	0.300	0.315
Fe^{3+}	0.000	0.202	0.047	0.195	0.124	0.170	0.000	0.000	0.000	0.230	0.000	0.000	0.174	0.088	0.091	0.053	0.140	0.000
Fe^{2+}	0.985	1.145	1.042	1.104	0.868	0.965	1.281	1.165	1.119	1.301	0.938	1.241	1.171	1.102	1.209	1.114	0.794	1.094
Mn	0.006	0.003	0.029	0.003	0.007	0.001	0.012	0.022	0.022	0.019	0.002	0.005	0.004	0.003	0.003	0.028	0.016	0.010
Mg	1.418	1.148	1.264	1.160	1.380	1.386	1.034	1.051	1.096	1.107	0.738	1.044	1.171	1.178	1.055	1.185	1.526	1.315
Na	0.069	0.057	0.015	0.057	0.058	0.034	0.009	0.021	0.019	0.040	0.031	0.004	0.028	0.042	0.021	0.029	0.024	0.032
K	0.804	0.791	0.909	0.703	0.771	0.817	0.914	0.926	0.910	0.841	0.738	0.789	0.901	0.791	0.892	0.894	0.864	0.899
Sum	7.737	7.793	7.824	7.716	7.729	7.817	7.788	7.778	7.780	7.834	7.532	7.676	7.829	7.732	7.813	7.823	7.789	7.808
X_{Mg}	0.590	0.501	0.548	0.512	0.614	0.590	0.447	0.472	0.495	0.460	0.440	0.457	0.500	0.517	0.466	0.515	0.658	0.546

$X_{Mg} = Mg/(Mg + Fe^{2+})$. Fe^{3+} is derived following the scheme of Droop (1987). Mineral symbols are after Kretz (1983).

TABLE 4

Muscovite compositions of mica schists from the Mayuan assemblage

Sample	N30-4	S4-1	S4-3	Z3-2	162-2	181-2	S4-1	S4-2	S4-3	D6-2	Z3-2	Z-3	162-2	181-1	181-2	G11-3	83-1	86-4
Textures	----------		inclusions		----------		----------					matrix						
Zones	Grt	Grt	Grt	St	Ky	Ky	Grt	Grt	Grt	St	St	St	Ky	Ky	Ky	Sil	Sil	Sil
SiO_2	46.77	48.02	47.50	46.11	47.44	46.38	45.35	48.34	45.55	47.02	46.66	46.89	47.10	46.81	47.02	48.08	46.63	46.42
TiO_2	0.30	0.27	0.24	0.30	0.37	0.45	0.57	0.45	0.39	0.25	0.21	0.48	0.36	0.00	0.33	0.60	1.39	1.39
Al_2O_3	36.85	35.86	37.00	36.82	35.54	36.74	36.10	36.78	35.77	37.31	38.73	35.32	33.33	38.80	39.56	37.92	36.36	34.00
FeO	1.14	0.87	3.47	0.82	0.90	1.33	0.91	0.94	0.87	0.74	1.19	1.12	1.55	1.04	1.00	1.23	0.71	0.91
MgO	0.66	0.61	1.63	0.74	0.56	1.02	0.53	0.57	0.52	0.56	0.39	0.55	1.25	0.53	0.59	1.00	0.53	0.97
Na_2O	1.37	0.61	0.38	0.45	0.01	0.80	0.75	0.47	0.73	1.56	0.86	1.59	0.90	0.71	0.61	0.37	0.48	0.84
K_2O	9.20	8.94	6.90	9.94	9.87	8.52	9.41	8.42	10.26	9.14	6.68	9.27	10.31	6.48	6.49	6.77	9.99	10.15
Totals	96.30	95.28	96.13	96.13	94.70	95.24	93.63	95.98	94.10	96.59	94.72	95.23	94.81	94.38	95.61	95.59	94.66	94.69
Si	3.057	3.145	3.067	3.074	3.140	3.045	3.048	3.127	3.060	3.056	3.035	3.103	3.153	3.047	3.020	3.080	3.055	3.103
Ti	0.015	0.013	0.012	0.015	0.018	0.022	0.029	0.022	0.020	0.012	0.010	0.024	0.018	0.000	0.016	0.029	0.068	0.070
Al^{IV}	0.943	0.855	0.933	0.926	0.860	0.955	0.952	0.873	0.940	0.944	0.965	0.897	0.847	0.953	0.980	0.920	0.945	0.879
Al^{VI}	1.889	1.914	1.884	1.906	1.913	1.889	1.908	1.932	1.893	1.915	2.005	1.859	1.783	2.025	2.016	1.940	1.863	1.782
Fe^{3+}	0.000	0.000	0.122	0.000	0.000	0.047	0.000	0.033	0.000	0.000	0.042	0.000	0.000	0.037	0.035	0.043	0.000	0.000
Fe^{2+}	0.062	0.048	0.052	0.045	0.050	0.020	0.051	0.014	0.049	0.040	0.018	0.062	0.087	0.016	0.015	0.018	0.039	0.051
Mg	0.064	0.060	0.061	0.072	0.055	0.100	0.053	0.055	0.052	0.054	0.038	0.054	0.125	0.051	0.056	0.095	0.052	0.097
Na	0.174	0.077	0.048	0.057	0.001	0.102	0.098	0.059	0.095	0.197	0.108	0.204	0.117	0.090	0.076	0.046	0.061	0.109
K	0.768	0.748	0.569	0.828	0.834	0.714	0.808	0.696	0.880	0.759	0.555	0.783	0.881	0.539	0.532	0.554	0.836	0.866
Sum	6.979	6.860	6.747	6.922	6.873	6.895	6.946	6.810	6.989	6.977	6.757	6.987	7.011	6.758	6.747	6.731	6.920	6.975
Pg	0.185	0.093	0.078	0.069	0.000	0.125	0.108	0.078	0.097	0.206	0.163	0.207	0.117	0.143	0.125	0.077	0.068	0.112
Ce	0.047	0.132	0.062	0.069	0.140	0.039	0.043	0.117	0.054	0.044	0.029	0.181	0.135	0.040	0.018	0.074	0.051	0.092
Ms	0.768	0.775	0.860	0.862	0.859	0.836	0.849	0.805	0.849	0.750	0.808	0.712	0.748	0.817	0.857	0.849	0.881	0.796

Fe^{3+} is derived following the scheme of Droop (1987). Minerals symbols are after Kretz (1983).

TABLE 5

Representative chlorite and staurolite analyses from pelitic schists

Sample	Z6-2	D4-1	D4-3	D6-3	Z6-2	D4-1	D4-3	D6-3	D6-2	Z3-2	Z-3	162-2	181-1	181-2
Mineral	Chlorite								Staurolite					
Textures	Matrix chlorite				Retrogressive chlorite				Porphyroblast					
SiO_2	24.15	24.78	24.38	24.35	25.62	25.86	25.66	25.52	27.96	26.36	27.89	27.70	28.22	27.72
TiO_2	0.05	0.04	0.00	0.01	0.10	0.03	0.00	0.03	0.41	0.38	0.45	0.41	0.47	0.62
$Al2O_3$	24.42	24.31	25.12	24.76	23.61	22.72	25.17	23.13	53.58	53.57	53.97	54.81	55.53	55.61
FeO	28.32	28.02	27.57	30.88	26.52	24.45	24.13	27.81	13.92	14.80	14.69	14.81	12.81	12.08
MnO	0.12	0.41	0.50	0.03	0.42	0.32	0.52	0.09	0.16	0.18	0.09	0.14	0.28	0.18
MgO	11.63	11.91	12.02	11.78	13.75	13.92	13.02	14.21	1.58	1.46	1.52	1.57	1.29	1.38
Na_2O	0.01	0.00	0.00	0.05	0.02	0.07	0.00	0.06	0.00	0.06	0.05	0.07	0.08	0.07
K_2O	0.01	0.00	0.03	0.04	0.06	0.00	0.03	0.03	0.00	0.00	0.00	0.00	0.00	0.07
Totals	88.71	89.48	89.62	89.51	90.10	87.37	88.54	90.88	97.61	96.81	98.66	99.51	98.68	97.73
Oxygens	14.0	14.0	14.0	14.0	14.0	14.0	14.0	14.0	46.0	46.0	46.0	46.0	46.0	46.0
Si	2.548	2.586	2.536	2.544	2.632	2.712	2.644	2.616	7.775	7.448	7.702	7.591	7.713	7.629
Ti	0.004	0.003	0.000	0.001	0.008	0.002	0.000	0.002	0.086	0.081	0.093	0.085	0.097	0.128
Al^{IV}	1.452	1.414	1.464	1.456	1.368	1.288	1.356	1.384	0.225	0.552	0.298	0.409	0.287	0.371
Al^{VI}	1.585	1.477	1.616	1.594	1.492	1.521	1.701	1.414	17.340	17.292	17.273	17.299	17.604	16.673
Fe^{2+}	2.499	2.445	2.398	2.490	2.279	2.145	2.079	2.384	3.237	3.497	3.393	3.394	2.928	2.781
Mn	0.011	0.036	0.044	0.003	0.037	0.028	0.045	0.008	0.038	0.043	0.021	0.032	0.065	0.042
Mg	1.829	1.854	1.863	1.834	2.105	2.176	1.999	2.171	0.655	0.615	0.626	0.641	0.525	0.566
Na	0.002	0.000	0.000	0.010	0.004	0.014	0.001	0.012	0.000	0.033	0.027	0.037	0.042	0.037
K	0.001	0.000	0.004	0.004	0.008	0.000	0.004	0.004	0.000	0.000	0.000	0.000	0.000	0.025
Sum	9.931	9.916	9.926	9.938	9.933	9.887	9.829	9.992	29.357	29.560	29.433	29.489	29.265	29.252
X_{Mg}	0.430	0.431	0.437	0.424	0.480	0.504	0.490	0.477	0.167	0.150	0.156	0.159	0.152	0.169

TABLE 6

Chemical compositions of hornblendes in amphibolites from the Mayuan assemblage

Sample	G11-2	83-2	86-3	100-4	107-2		G11-2	83-2	86-3	100-4	1072
SiO_2	43.07	42.61	43.39	42.82	43.29	Si	6.330	6.285	6.291	6.290	6.340
TiO_2	1.02	1.41	1.33	1.44	1.06	Ti	0.113	0.156	0.145	0.159	0.117
Al_2O_3	14.18	13.19	14.05	13.61	13.55	Al^{IV}	1.670	1.715	1.709	1.710	1.660
FeO	10.64	10.87	9.60	13.80	9.60	Al^{VI}	0.787	0.479	0.692	0.647	0.680
MnO	0.04	0.80	0.12	0.04	0.60	Fe^{3+}	0.419	0.586	0.542	0.285	0.596
MgO	10.90	10.47	11.56	10.00	11.10	Fe^{2+}	1.308	1.341	1.164	1.695	1.176
CaO	11.24	11.09	11.04	11.92	11.12	Mn	0.005	0.100	0.015	0.005	0.074
Na_2O	1.98	1.71	1.90	2.10	1.58	Mg	2.388	2.301	2.498	2.189	2.423
K_2O	0.50	0.63	0.59	0.78	0.42	Ca	1.770	1.753	1.715	1.876	1.745
						Na^{M4}	0.210	0.184	0.229	0.124	0.189
						Na^{A}	0.354	0.305	0.305	0.474	0.260
						K	0.094	0.119	0.109	0.146	0.079
Totals	97.36	98.06	98.55	99.09	97.73	Sum	15.45	15.42	15.41	15.60	15.34

Fe^{3+} is derived following the scheme of Droop (1987).

garnet-producing reaction. Therefore, the appearance of garnet in the garnet zone is most probably related to the continuous Fe-Mn-Mg reaction

$$\text{chlorite} + \text{muscovite} + \text{quartz} = \text{garnet} + \text{biotite} + H_2O \quad (2)$$

This reaction accounts for the decrease in chlorite and muscovite and increase in biotite contents within the garnet zone, compared with the chlorite-biotite zone.

Staurolite-in reactions.–The incoming of staurolite should be related to biotite-producing and chlorite- and muscovite-consuming reactions, because the staurolite zone is marked by a strong increase in the modal abundance of biotite, at the expense of chlorite and muscovite. AFM-phase compatibilities (fig. 6) suggest that the development of staurolite may be related either to the continuous FeMg reaction

$$\text{chlorite} + \text{muscovite} + \text{quartz} = \text{staurolite} + \text{biotite} + H_2O \quad (3)$$

or to the model discontinuous, garnet-consuming reaction

$$\text{garnet} + \text{chlorite} + \text{muscotive} + \text{quartz} = \text{staurolite} + \text{biotite} + H_2O \quad (4)$$

The textural relations observed in the rocks incorporate the model reaction (3), because: (1) the modal abundance of garnet has not been obviously decreased within the staurolite zone; (2) in thin sections, garnet and staurolite grains show straight mutual contacts, and no reaction relationship between them was observed; and (3) relict chlorite and muscovite have been found within staurolite grains.

Kyanite-in reactions.–The AFM topologies (fig. 6) suggest that kyanite may have developed either through the chlorite-consuming reaction

$$\text{chlorite} + \text{muscovite} = \text{kyanite} + \text{biotite} + \text{quartz} + H_2O \quad (5)$$

or through the garnet-consuming reaction

$$\text{garnet} + \text{muscovite} = \text{kyanite} + \text{biotite} + \text{quartz} \quad (6)$$

or through the following staurolite-consuming reactions

$$\text{staurolite} + \text{muscovite} + \text{quartz} = \text{kyanite} + \text{biotite} + H_2O \quad (7)$$

$$\text{staurolite} + \text{quartz} = \text{kyanite} + \text{garnet} + H_2O \quad (8)$$

However, textural observations do not suggest production of kyanite through reactions (6), (7), and (8), because garnet, staurolite, and kyanite in the kyanite zone display equilibrium textures, with regular and planar interfaces. Therefore, the entrance of kyanite is most probably related to reaction (5).

Sillimanite-in reactions.–The AFM compatibilities (fig. 6) allow the following Al_2SiO_5-producing reactions to form sillimanite:

$$\text{chlorite} + \text{muscovite} = \text{sillimanite} + \text{biotite} + \text{quartz} + H_2O \quad (9)$$

$$\text{garnet} + \text{muscovite} = \text{sillimanite} + \text{biotite} + \text{quartz} \quad (10)$$

$$\text{staurolite} + \text{muscovite} + \text{quartz} = \text{sillimanite} + \text{biotite} + H_2O \quad (11)$$

$$\text{staurolite} + \text{quartz} = \text{sillimanite} + \text{garnet} + H_2O \quad (12)$$

$$\text{kyanite} = \text{sillimanite} \quad (13)$$

Microstructural observations in the Mayuan pelitic schists suggest production of sillimanite through reactions (10) and (13). These microstructures include: (1) the appearance of fibrolitic sillimanite + biotite symplectite forming pseudomorphs after garnet porphyblasts, in which minor relict garnet crystals have been observed; and (2) presence of relict kyanite observed as inclusions within biotite crystals, implying the production of biotite + sillimanite was associated with the kyanite-consuming reaction. Reactions (11) and (12) may have occurred, but their reaction textures were not preserved.

Retrograde hydration reactions.–The retrogressive chlorite and muscovite may have developed through the following reactions:

$$\text{garnet} + \text{biotite} + H_2O = \text{chlorite} + \text{muscovite} + \text{quartz} \quad (14)$$

$$\text{staurolite} + \text{biotite} + H_2O = \text{chlorite} + \text{muscovite} + \text{quartz} \quad (15)$$

$$\text{kyanite} + \text{biotite} + \text{quartz} + H_2O = \text{chlorite} + \text{muscovite} \quad (16)$$

$$\text{sillimanite} + \text{biotite} + \text{quartz} + H_2O = \text{chlorite} + \text{muscovite}. \quad (17)$$

P–T evolution constrained by petrogenetic grids.–The petrogenetic (or P–T) grids of metapelites have been investigated using essentially two different approaches. Some workers have calculated stable K_2O–FeO–MgO–Al_2O_3–SiO_2– H_2O (KFMASH) system reactions using experimentally based internally consistent thermodynamic datasets for the mineral endmembers, combined with estimated solution models (Spear and Cheney, 1989; Powell and Holland, 1990; Powell, Holland, and Worley, 1998), whereas others have established reaction grids based on repeated occurrences of natural mineral assemblage sequences, combined with Schreinemakers' rules (Harte, 1975; Thompson, 1976; Pattision and Tracy, 1991). In this study, the P–T grid of Powell, Holland, and Worley (1998) is used because it was constructed based on the updated thermodynamic data and solution models, and more importantly, it agrees well with the sequence of mineral reactions deduced for the Mayuan pelitic schists.

Figure 7 is a P–T pseudosection of the KFMASH grid of Powell, Holland, and Worley (1998), but extension for low-temperature domains has been made to take into account the M4 mineral assemblage observed in the Mayuan pelitic schists. This KFMASH (+ muscovite + quartz + H_2O) grid, built up for a common pelitic AFM composition (Al_2O_3 = 41.89, MgO = 18.19, FeO = 27.29, and K_2O = 12.63 (in mol)),

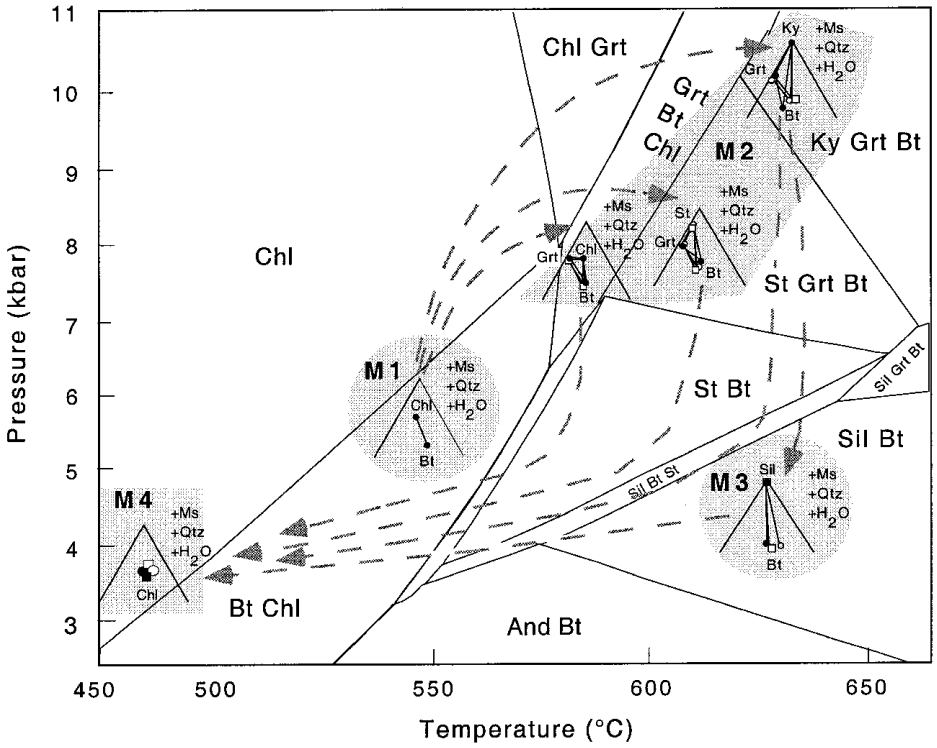

Fig. 7. P–T pseudosection for a portion of the KFMASH system (slightly modified after Powell, Holland and Worley (1998)) showing the qualitative P–T path of the Mayuan metapelitic schists constrained by the sequence of mineral assemblages. Mineral symbols are after Kretz (1983).

shows a prograde sequence of mineral assemblages similar to those observed in the Mayuan pelitic schists. For example, the domains chlorite + biotite, garnet + biotite + chlorite, staurolite + garnet + biotite, kyanite + garnet + biotite, sillimanite + biotite and chlorite, each of which is with muscovite + quartz + H_2O in excess, can be used to show the M1 assemblage, the M2 assemblages of the garnet, staurolite, and kyanite zones, the M3 assemblage of sillimanite zone, and the M4 assemblage in the Mayuan pelitic schists, respectively (fig. 7). As seen in figure 7, the equilibrium P–T conditions of the garnet + biotite, staurolite + garnet + biotite and kyanite + garnet + biotite domains are higher than that of the chlorite + biotite domain, and thus, the transition from M1 to M2 represents a P- and T-increasing process. The sillimanite + biotite domain is characterized by much lower pressure than kyanite + garnet + biotite domain, but both domains may have a similar temperature range. Therefore, the transition from M2 to M3 may represent a decompression or near-isothermal decompression process (fig. 7). The chlorite domain has a wide P–T scope, but the M4 assemblage of chlorite + muscovite should be located in its lower pressure area (<4 kb), which defines a relatively low temperature range (<500°C; fig. 7). Taken together, a decompression-type clockwise P–T path has been qualitatively inferred from the evolutionary sequence of mineral assemblages of different metamorphic stages in the Mayuan pelitic schists (fig. 7). The quantitative P–T trajectory cannot be defined from this grid because of the lack of insufficient critical reactions and compisitional information.

THERMOBAROMETRY

P–T conditions of M_1 and M_2.–Both the M_1 and M_2 mineral assemblages in pelitic schist contain garnet, muscovite, biotite, plagioclase, and quartz, and thus their equilibrium P–T estimates were calculated by simultaneous solution of the garnet–biotite thermometer:

almandine + phlogopite = pyrope + annite,

and the garnet–muscovite–biotite–plagioclase barometers:

almandine + grossular + muscovite = anorthite + annite

and

pyrope + grossular + muscovite = anorthite + annite

using the TWEEQU software package of Berman (1991). TWEEQU incorporates the internally consistent thermodynamic data of Berman (1988, 1990), Mäder and Berman (1992), and McMullin, Berman, and Greenwood (1991). Activity–composition relations for garnet, muscovite, biotite, and plagioclase were computed using the models of Berman (1990), Chattrjee and Forese (1975), McMullin, Berman, and Greenwood (1991), and Furhman and Lindsley (1988), respectively. Overall uncertainties for the TWEEQU calculations are difficult to assess quantitatively because they also include errors in electron microprobe analysis, solution models, and thermodynamic properties. We adopt a maximum "aggregate uncertainty" for our TWEEQU results of ±1.0 kb and 50°C, based on earlier suggestions by Essene (1989) for single thermobarometers. To minimize the effect of cationic diffusional exchange on mineral compositions and thermobarometric calculations, P–T estimates of M_1 are based on the inclusion-rich core compositions of large garnet grains and the compositions of the enclosed plagioclase, and muscovite and biotite which themselves are surrounded by plagioclase and quartz inclusions, whereas P–T estimates of M_2 are based on the inclusion-free rim compositions of garnet and matrix biotite, along with muscovite and plagioclase compositions from those samples that are devoid of retrogressive chlorite, muscovite (sericite), and epidote around garnet and plagioclase. The results of P–T estimates for M_1 and M_2 are shown in figures 8 and 9. Six pelitic schist samples display good intersample P–T compatibility and yield pressures between 5.5 to 6.0 kb and temperature between 450° to 500°C for the M_1 stage (fig. 8). These P–T estimates might be influenced by undetected compositional heterogeneity and thus only represent approximate conditions of M_1, whereas the "real" P–T conditions of M_1 cannot be constrained because of the lack of high-resolution mineral compositional mapping. The P–T conditions estimated for the M_2 stage are 6.0 to 7.0 kb and 550° to 600°C for the garnet zone, 6.0 to 7.7 kb and about 600°C for the staurolite zone, and 11.0 to 11.5 kb and about 600°C for the kyanite zone (fig. 9). These P–T conditions can be approx correlated to those constrained by the P–T grid of pelites (fig. 7). The P–T conditions of the kyanite zone were also computed by simultaneous solution of the garnet–biotite thermometer and the garnet–kyanite–anorthite–quartz barometer using the TWEEQU program. The temperatures yielded by the solution of these two geothermobarometers are also around 600°C, but the pressures are about 2 kb higher than those yielded by the simultaneous solution of the garnet–biotite thermometer and garnet–muscovite–biotite–plagioclase barometer (fig. 10). The relatively high pressures obtained for the kyanite zone are consistent with high grossular contents analyzed from the garnets and its tectonic contact with the staurolite zone.

P–T conditions of M_3.–The P–T conditions of the M_3 assemblages in pelitic schist cannot be estimated using the above geothermobarometers because of the lack of garnet in sillimanite-bearing rocks. Instead, the muscovite–biotite geothermometer of Hoisch

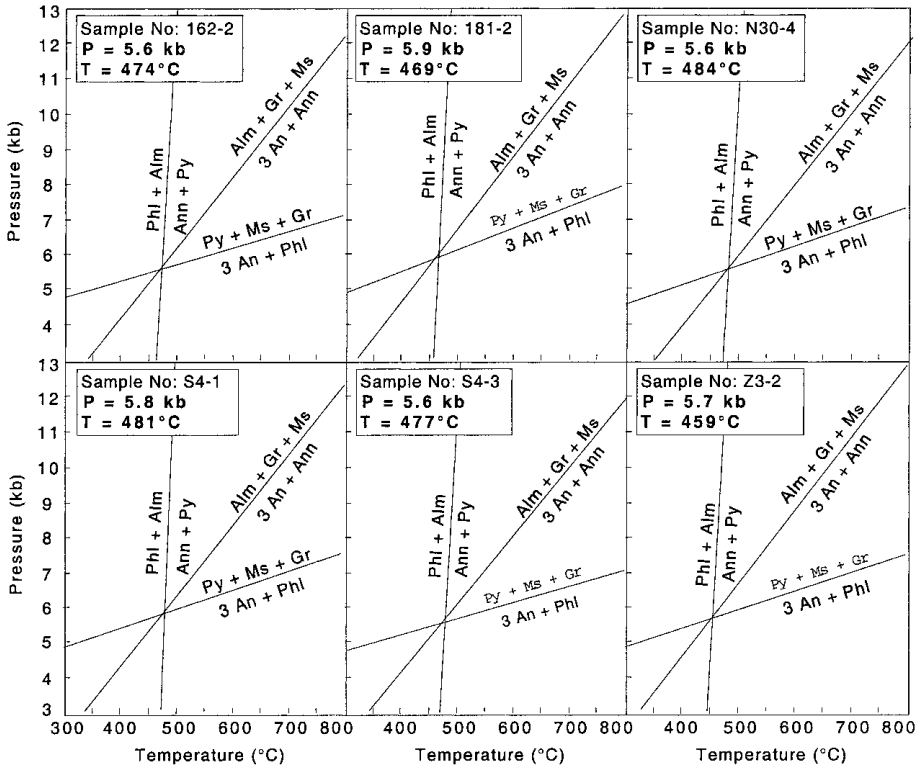

Fig. 8. P–T estimates for the M_1 stage computed by simultaneous solution of the garnet–biotite thermometer and the garnet–muscovite–biotite–plagioclase barometer using the TWEEQU software package of Berman (1991).

(1989) was used and gives temperatures ranging from 570° to 610°C (table 7). The P–T conditions of M_3 can also be estimated from epidote amphibolite associated with sillimanite-bearing schist by using the hornblende–plagioclase thermometer of Holland and Blundy (1994) and the hornblende–plagioclase geothermobarometer of Plyusnina (1982). The former yielded a temperature of 590° to 620°C (table 7), whereas the latter yielded a pressure of 4.0 to 4.5 kb and a temperature of 590° to 625°C (table 7). The temperature estimates by the thermometers of Holland and Blundy (1994) and Plyusnina (1982) are similar to those by the muscovite–biotite thermometer of Hoisch (1989). The relatively low pressure estimated for M_3 is consistent with pressure constraints on the M_3 phase assemblage in P–T grid of pelites (fig. 7).

P–T conditions of M_4.–The temperatures of M_4 can be semi-quantitatively estimated using rim compositions of garnet surrounded by retrogressive chlorites and the garnet–chlorite thermometer of Dickenson and Hewitt (1986) combined with garnet activity models of Hodges and Spear (1982), Ganguly and Saxena (1984), and Berman (1990). The temperatures calculated using the Berman (1990) correction are consistent with those calculated using Hodges and Spear (1982) correction and are preferred because they are based on recent experimental and calorimetric data. The thermometer using the garnet activity model of Berman (1990) produced a temperature between 335° to 410°C for the M_4 stage at a reference pressure of 3.5 kb (fig. 11). The temperature estimates by the garnet–chlorite thermometers are little influenced by reference pressures because, as seen in figure 11, the P–T curves of the thermometer are nearly parallel to the Y

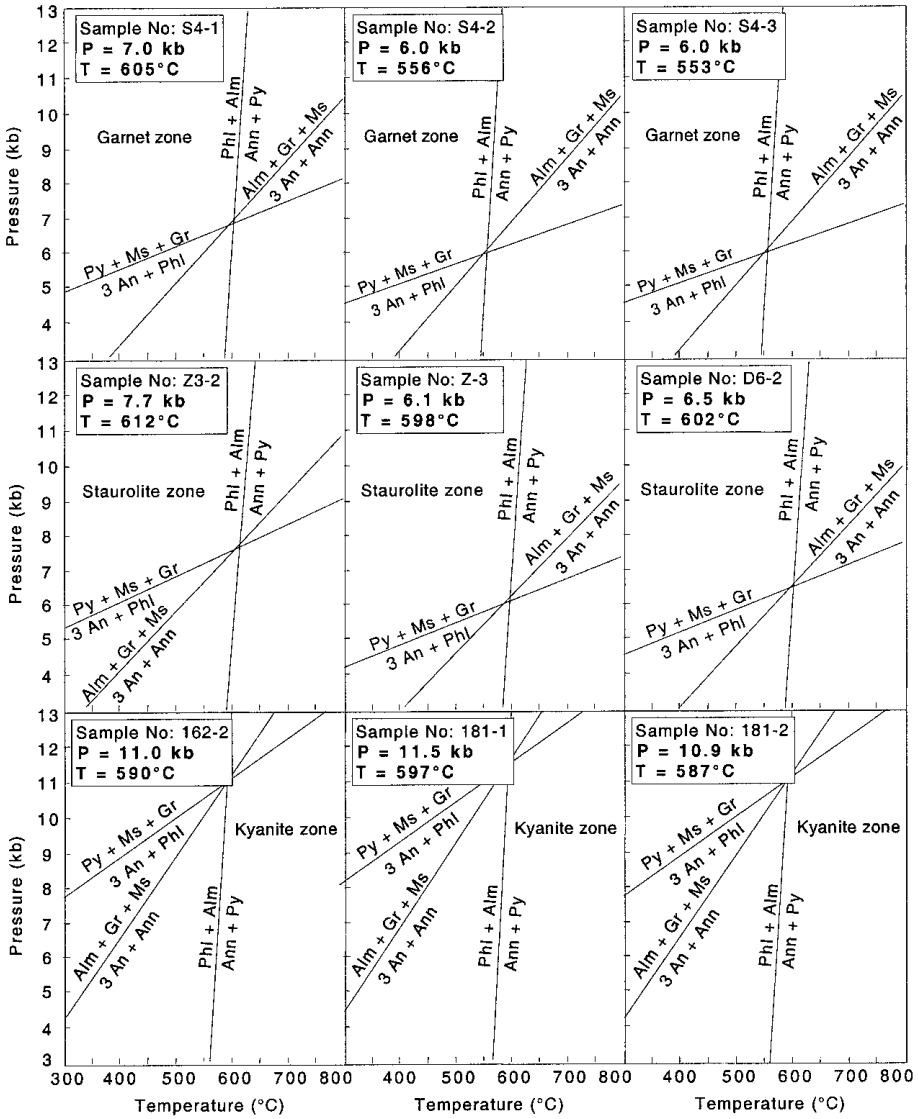

Fig. 9. P–T estimates for the M_2 stage computed by simultaneous solution of the garnet–biotite thermometer and the garnet–muscovite–biotite–plagioclase barometer using the TWEEQU software package of Berman (1991).

(Pressure) axe. The pressure of M_4 cannot be quantitatively estimated because of the lack of suitable barometers, but considering the characteristics of the M_4 mineral assemblage and the pressure of M_3, it should not be more than 4.0 kb.

P–T PATH

Relations between mineral growth and deformational episodes, mineral compositions and thermobarometric calculations for the Mayuan assemblage define a near-isothermal decompressional clockwise P–T path (fig. 12), which is consistent well with the P–T path (fig. 7) qualitatively reconstructed based on the sequence of mineral

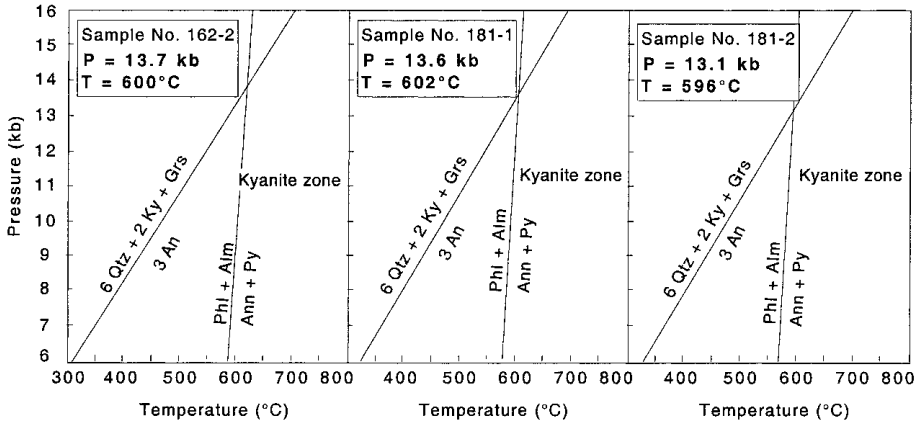

Fig. 10. P–T estimates for the M_2 stage (kyanite zone) computed by simultaneous solution of the garnet–biotite thermometer and the garnet–kyanite–plagioclase–quartz barometer using the TWEEQU software package of Berman (1991).

assemblages and history of metamorphic reactions in the petrogenetic grid of pelites. Some uncertainties for the P–T estimates of the M_3 and late retrograde metamorphic stages may exist because of the lack of suitable geothermobarometry, but large parts of the path are well constrained by textural relations and quantitative P–T estimates.

The M_1 mineral assemblages from different lithological units and the P–T estimates from pelitic schist suggest that the Mayuan assemblage experienced an early phase of greenschist-facies metamorphism (M_1) during the first deformational episode (D_1). This phase of metamorphism may be related to thickening during the initial stage of orogenesis. Following M_1, the Mayuan assemblage underwent peak metamorphism (M_2), resulting in the development of prograde metamorphic zones in the area; chlorite–biotite, garnet, and staurolite zones developed in the upper part of the crust, whereas the

TABLE 7

P–T estimates for M_3 using the muscovite–biotite thermometer (Hoisch, 1989) and the hornblende–plagioclase thermobaromers of Holland and Blundy (1994) and (Plyusnina, 1982).

Geothermobarometers	Mu–Bt	Hbl–Pl	Hbl–Pl	Hbl–Pl
Sample	T_1 (°C)	T_2(°C)	T_3 (°C)	P_1 (kbar)
G11-3	589			
83-1	578			
86-4	609			
G11-2		597	590	4.4
83-2		614	590	4.2
86-3		607	625	4.2
100-4		619	595	4.3
107-2		592	615	4.5

T_1, Hoisch (1989); T_2, Holland and Blundy (1994); T_3/P_1, Plyusnina (1982).

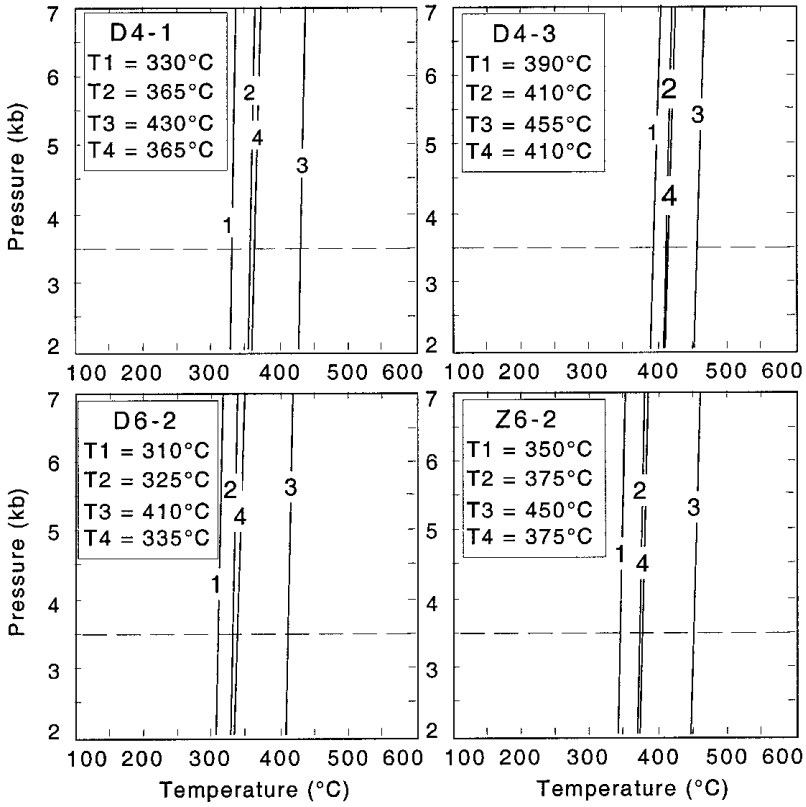

Fig. 11. P–T estimates for M_4 using the garnet–chlorite thermometer of Dickenson and Hewitt (1986) with garnet activity models of Hodges and Spear (1982), Ganguly and Saxena (1984) and Berman (1990). 1-Dickson and Hewitt (1986); 2-Hedges and Spear (1982); 3-Gangly and Saxon (1984); 4-Barman (1990).

kyanite zone developed in the lower part of crust. The P–T conditions of 10 to 11 kb and 600°C estimated for the kyanite zone indicate amphibolite to amphibolite–eclogite transitional facies metamorphism for this zone during M_2. This implies that the metamorphosed crust has been doubly thickened during M_2. The relatively high pressure metamorphism is supported by recent discovery of jadeite-bearing glaucophane blueschists along the Jiangshan–Shaoxing suture (Zhang, 1994). The P–T conditions of the jadeite-bearing glaucophane schists were estimated at 15 to 20 kb and >250°C (Zhang, 1994). Further support is given by the presence of high b0 phengite in the kyanite-bearing schists from the Mayuan assemblage (Gao, 1991). The P–T conditions of 4.0 to 4.5 kb and 590° to 625°C estimated for M_3 suggest that the lower part of metamorphic crust (kyanite zone) experienced isothermal decompression after thickening. The isothermal decompression indicates rapid exhumation relative to the rate of thermal relaxation (England and Thompson, 1984). It is uncertain if the chlorite–biotite, garnet, and staurolite zones also underwent M_3 or move directly toward M_4 conditions. Decompression was followed by greenschist facies retrogression (M_4). Evidence for this regional retrogression is indicated by a number of hydration reactions, mainly involving the replacement of garnet and staurolite by chlorite and muscovite, kyanite and sillimanite by sericite, hornblende by chlorite, and plagioclase by epidote. Considering the relationships between the metamorphic and deformational episodes, the M_4 stage most likely

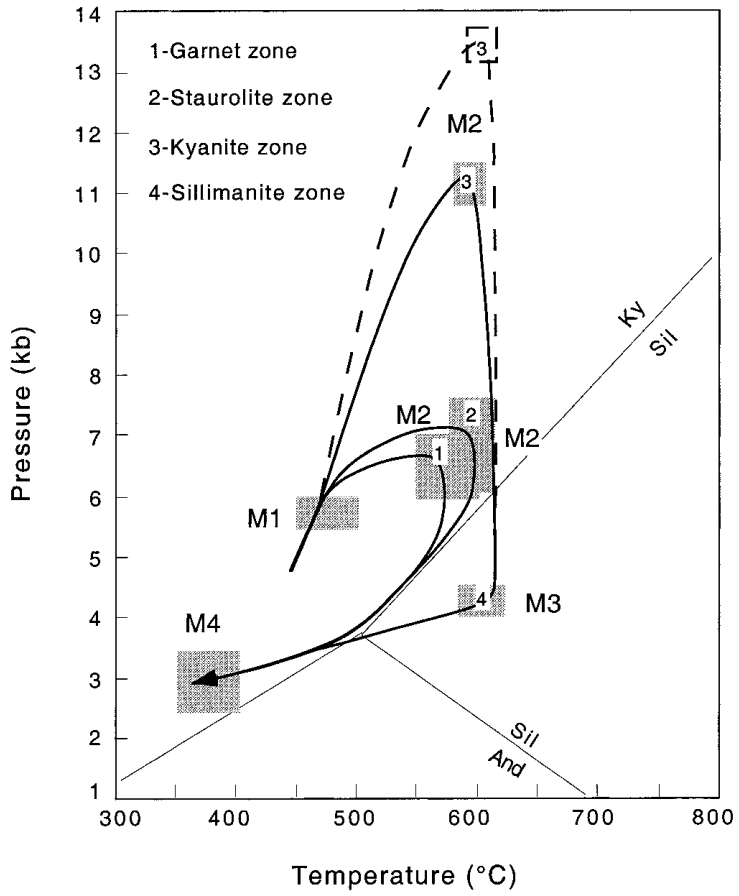

Fig. 12. P–T path of the Mayuan assemblage. The dashed line shows a portion of the P–T path based on the P–T conditions of the kyanite zone calculated by simultaneous solution of the garnet–biotite thermometer and the garnet–kyanite–anorthite–quartz barometer using the TWEEQU program.

occurred when the region was being exhumed to a shallow level, and hence, the pressures and temperatures were decreasing.

TECTONIC IMPLICATION AND DISCUSSION

The sequence of mineral assemblages, metamorphic reaction history, and estimated clockwise P–T path (figs. 7 and 12) for the Mayuan assemblage in the Cathaysia Block reflect tectonothermal processes characterized by initial crustal thickening ($M_1 + M_2$), subsequent rapid exhumation (M_3), and final cooling (M_4). This sequence of tectonothermal processes is consistent with a continent–continent collisional model (England and Thompson, 1984; Thompson and England, 1984; Brown, 1993). Thus, the tectonothermal evolution of the Mayuan assemblage provides new evidence for the tectonic model that the South China craton developed as a result of the amalgamation of the Cathaysia and Yangtze blocks.

The collisional event that resulted in the amalgamation of the Cathaysia and Yangtze blocks was previously considered to be of terminal Mesoproterozoic age (Shui, 1987; Li, Gui, and Yu, 1992; Zhou and others, 1993; Li, X, 1994; Li, Z. X., 1998), which led Li, Zhang, and Powell (1995, 1996) to correlate it with the Grenville event and to

suggest that the South China craton was an important part of Rodinia, lying between East Australia and western North America. Recent isotopic dating, however, suggests a Neoproterozoic rather than Mesoproterozoic age for this collisional event. An older limit on the timing of collision is provided by the age of 1034 ± 24 Ma for ophiolitic rocks along the Jiangshan–Shaoxing suture (Chen and others, 1991). The K–Ar age of 866 ± 14 Ma for glaucophanes from the blueschists within the collision zone was interpreted as their peak metamorphic crystallization age (Ma and Wang, 1994). In addition, peraluminous (S-type) granites within the collisional zone have yielded U–Pb zircon ages of around 825 Ma (Li, 1999), which are considered to represent the timing of exhumation of metamorphosed terranes because these S-type granites were derived from the decompressional melting of meta-sedimentary rocks during tectonic exhumation following the collisional thickening (Zhao, Sun, and He, 1994a; Li, 1999). Similar metamorphic crystallization and cooling ages have also been obtained from the Mayuan assemblage in the Cathaysia Block. Syn-tectonic granites from the Mayuan assemblage yielded U–Pb zircon ages of ~868 Ma (Shui, 1987), and hornblendes from amphibolites were dated using the K–Ar methods at around 844 Ma (Shui, 1987). Li (1989) obtained U–Pb ages of ~868 Ma from metamorphic zircons in paragneisses of the Mayuan assemblage. All these isotopic data suggest that the amalgamation of the Yangtze and Cathaysia blocks occurred at around 870 to 820 Ma. Orogenic activity of this age is not known from either eastern Australia or western North America and argues against placing the South China craton between these continental segments in any Rodinian reconstruction. Paleomagnetic data by Zhang and Piper (1997) for the Neoproterozoic Sinian strata from the Yangtze Block also argue against placing the South China craton between eastern Australia and western North America.

Available geologic data indicate that although the South China craton did not lie off eastern Australia, it was connected to Australia. The unmetamorphosed Sinian succession in the South China craton is similar in age and character to the sequences in the Centralian Superbasin and Adelaide Fold Belt of central and eastern Australia respectively (Preiss and others, 1993). Li and others (1999) have dated mafic/ultramafic intrusives into the Sibao Group by U/Pb SHRIMP zircon at 828 ± 7 Ma. This is identical to the age of the basaltic dikes in southcentral Australia (Wingate and others, 1998). Combining this data with limited paleomagnetic constraints (Zhang and Piper, 1997; Li and Powell, 1999), we consider South China was located off northern Australia in the Neoproterozoic. This would place South China along an ocean flanking margin of Rodinia rather than in an intra-cratonic setting enabling mid-Neoproterozoic collision of the Yangtze and Cathaysia blocks.

The deformational and metamorphic data along with lithological and geochronological considerations allow the development of the following tectonic model for the amalgamation of the Cathaysia and Yangtze blocks.

1. In the Mesoproterozoic, the Yangtze and Cathaysia blocks were separate continental fragments. The Yangtze Block consisted of basement of the Paleoproterozoic Kangding and Mesoproterozoic Sibao assemblages and cover of Early Neoproterozoic Banxi assemblage, whereas the Cathaysia Block consisted of basement of the Paleoproterozoic Badu assemblage and cover of Mesoproterozoic to Early Neoproterozoic Mayuan assemblage. Separating the two continental blocks was an ocean lithosphere, represented by the approx 1000 Ma ophiolite suite exposed along the Jiangshan–Shaoxing suture (fig. 13A).

2. Collision of the Yangtze and Cathaysia blocks occurred in the Neoproterozoic (870-820 Ma). Initially, the collision caused folding and moderate crustal thickening, resulting in the first phase of deformation (D_1) and greenschist facies metamorphism (M_1, fig. 13B).

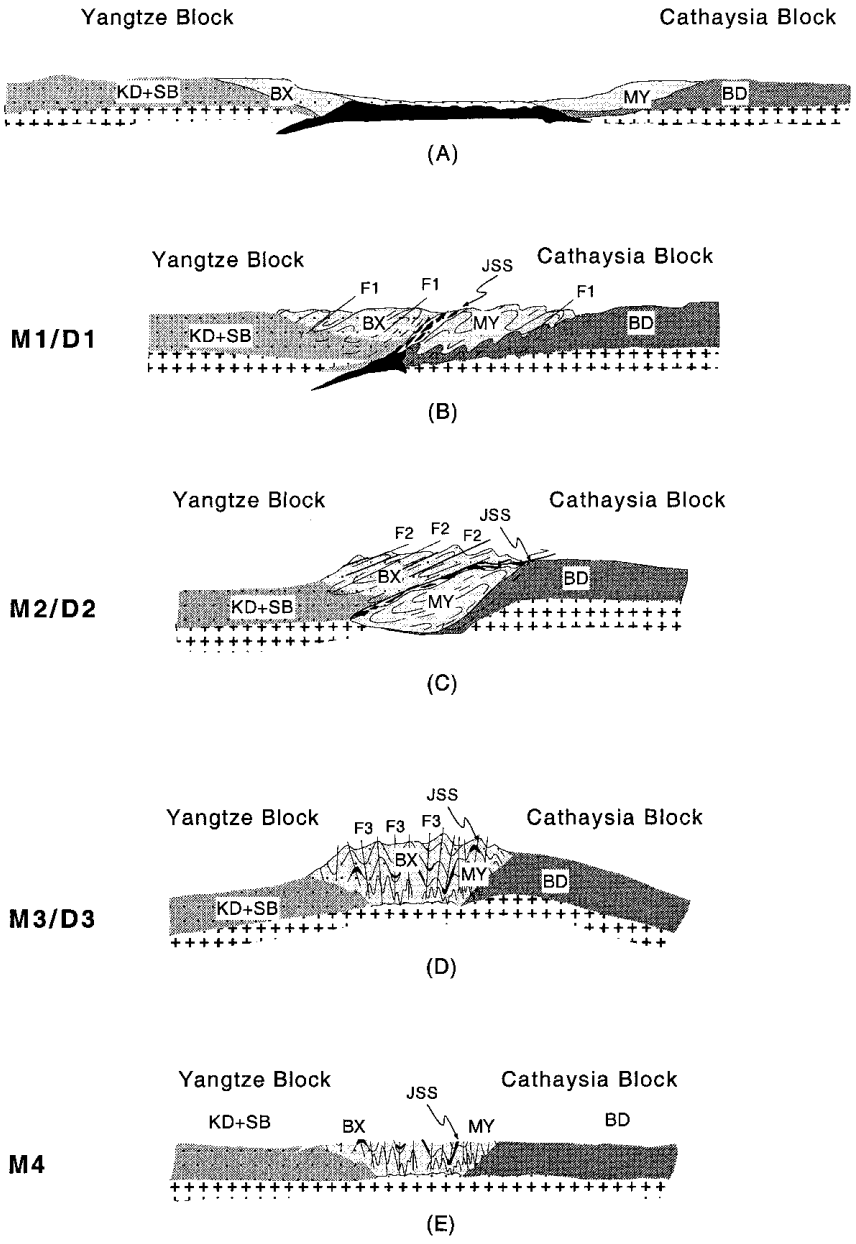

Fig. 13. A series of schematic sections showing the suggested tectonothermal evolution for assembly of the Cathaysia and Yangtz blocks. Abbreviation: BD–Badu assemblage; BX–Banxi assemblage; JSS–Jiangshan–Shaoxing suture; KD–Kangding assemblage; MY–Mayuan assemblage; SB–Sibao assemblage.

3. The further crustal thickening associated with folding and thrusting of the Banxi assemblage over the Cathaysia Block along the Jiangshan–Shaoxing suture resulted in the second phase of deformation (D_2) and development of prograde metamorphic zones (M_2) in the Mayuan assemblage: the chlorite–biotite, garnet, and staurolite zones in the upper level of the crust, whereas the kyanite zone in the lower level of crust (fig. 13C).

4. Following the prograde metamorphism (M_2), the thickened crust underwent rapid exhumation, represented by isothermal decompression metamorphism (M_3) and D_3 deformation, which resulted in folding of both the prograde metamorphic zones and the Jiangshao–Shaoxing suture (fig. 13D). Minor ophiolites have been reported from some other faults that extend in parallel to the Jiangshan–Shaoxing suture in the Yangtze Block (for example the Jingdezheng–Yifeng Fault; Yang and Fan, 1994). These faults may represent either different parts of the same folded Jiangshao–Shaoxing suture (fig. 13D) or secondary faults within the suture zone.

5. Finally, retrogressive cooling (M_4) occurred with the further exhumation of the metamorphosed crust to a shallow level (fig. 13E).

Following the amalgamation of the Cathaysia and Yangtze blocks, the South China craton underwent a rifting event (Li, 1999; Li and others, 1999), which resulted in a widespread intrusion of mafic to ultramafic dikes at around 830 to 820 Ma (Li and others, 1999) followed by basin subsidence in the South China craton for the remainder of the Neoproterozoic and early Paleozoic (Li, 1999). This rifting with associated magmatic activity may have been driven by post-collisional extensional collapse (Dewey, 1988) or mantle plumes (Li and others, 1999). With the further development of the rifting, the Cathaysia and Yangtze blocks (South China craton) rifted away from Northern Australia and then drifted with East Gondwana to amalgamate with West Gondwana by mid-Cambrian to form the Gondwana supercontinent (Zhao and others, 1996). The Early Paleozoic deformation and metamorphism within the South China craton (for example Wuyi–Yunkai assemblage) may be related to this tectonic event, whereas the Jurassic metamorphism and deformation within the craton (for example Pingtan–Dongshan assemblage) may be related to the breakup of Gondwana or/and the final assembly of the major China cratonic blocks (Metcalfe, 1996; Zhao and others, 1996).

ACKNOWLEDGMENTS

Financial support from the Tectonics Special Research Centre (TSRC) at Curtin University and Education Foundation of China (EFC) is gratefully acknowledged. Zhengxiang Li and Ian C. Fitzsimons provided thoughtful discussions. We thank Mark T. Brandon, Jay J. Ague, and two anonymous reviewers for their critical but constructive comments that led to substantial changes and improvements in this manuscript. This is Tectonics Special Research Centre publication no. 57.

References

Berman, R. G., 1988, Internally consistent thermodynamic data for minerals in the system Na_2O–K_2O–CaO–MgO–FeO– Fe_2O_3–Al_2O_3– SiO_2–TiO_2–H_2O–CO_2: Journal of Petrology, v. 29, p. 445–522.

——— 1990, Mixing properties of Ca–Mg–Fe–Mn garnets: American Mineralogist, v. 75, p. 328–344.

——— 1991, Thermobarometry using multi-equilibrium calculations: a new technique, with petrological applications: Canadian Mineralogist, v. 29, p. 833–855.

Bohlen, S. R., 1987, Pressure-temperature-time paths and tectonic model for the evolution of granulites: Journal of Geology, v. 95, p. 617–632.

——— 1991, On the formation of granulites: Journal of Metamorphic Geology, v. 9, p. 223–229.

Brown, M., 1993, P–T–t evolution of orogenic belts and the causes of regional metamorphism: Journal of Geological Society, London, v. 150, p. 227–241.

Chatterjee, N. D., and Froese, E., 1975, A thermodynamic study of the pseudobinary join muscovite–paragonite in the system $KAlSi_3O_8$–$NaAlSi_3O_8$– Al_2O_3–SiO_2–H_2O: American Mineralogist, v. 60, p. 985–993.

Chen, B., 1997, Petrographic evidence and tectonic significance of two phases of metamorphism in the sillimanite- and garnet-bearing mica schists from Pingtan–Dongshan metamorphic zone, Eastern Fujian, China: Acta Petrologica Sinica, v. 13, p. 380–394 (in Chinese).

Chen, J., Foland, K. A., Xing, F., Xu, X., and Zhou, T., 1991, Magmatism along the southeast margin of the Yangtze block: Precambrian collision of the Yangtze and Cathaysia blocks of China: Geology, v. 19, p. 815–818.

Dewey, J. F., 1988, Extensional collapse of orogens: Tectonics, v. 7, p. 1123–1139.

Dickenson, M. P., and Hewitt, D., 1986, A garnet–chlorite geothermometer: Geological Society of America Abstracts with Programs, v. 18, p. 584.

Dong, S. B., 1986, Metamorphism and crustal evolution of China, *in* Dong, S. B., editor, Relationships between metamorphism and crustal revolution in China: Special Issue of China Geology–Petrology, Mineralogy and Geochemistry, v. 4, p. 214–225.

Droop, G. T. R., 1987, A general equation for estimating Fe^{3+} concentrations in ferromagnesian silicates and oxides from microprobe analyses, using stoichiometric criteria: Mineralogical Magazine, v. 51, p. 413–415.
England, P. C., and Thompson, A. B., 1984, Pressure-temperature-time paths of regional metamorphism, I. Heat transfer during the evolution of regions of thickened continental crust: Journal of Petrology, v. 25, p. 894–928.
Essene, E. J., 1989, The current status of thermobarometry in metamorphic rocks, *in* Daly, J. S., Cliff, R. A., and Yardley, B. W. D., editors, Evolution of metamorphic belt: Geological Society Special Publication, v. 43, p. 1–44.
Fuhrman, M. L., Lindsley, D. H., 1988, Ternary–feldspar modelling and thermometry: American Mineralogist, v. 73, p. 201–216.
Gan, X. C., Zhao, F. Q., Li, H. M., Tang, X. X., and Huang, J. Z., 1993, Grain zircon U–Pb ages from volcanic rocks for Banxi Group in Hunan, *in* Isotopic Committee of the Geological Society of China, editor, The evolution of crust and mantle, diagenesis and mineralization isotopic geochemistry: Beijing, Seismological Press, p. 10–11.
Ganguly, J., and Saxena, S. K., 1984, Mixing properties of aluminosilicate garnets: constraints from natural and experimental data, and applications to geothermo-barometry: American Mineralogist, v. 69, p. 88–97.
Gao, T. J., 1991, Two significant terrane boundaries in the southeast coast of China: Fujian Geology, v. 10, p. 1–15 (in Chinese).
Han, F., 1994, The geochronological study of the Sibao Group in the southern margin of Jiangnan terrane: Acta Geoscienita Sinica, Bulletin of the Chinese Academy of Geological Sciences, v. 30, p. 43–48 (in Chinese).
Harley, S. L., 1989, The origins of granulites: a metamorphic perspective: Geological Magazine, v. 126, p. 215–247.
Harte, B., 1975, Determination of a pelite petrogenetic grid for the eastern Scottish Dalradian: Carnegie Institution of Washington, Yearbook, v. 74, p. 483–446.
He, T. X., and Zhang, X. Z., 1989, Phanerozoic metamorphism and crustal evolution of the southeastern part of China: Journal of Southeast Asian Earth Sciences, v. 3, p. 321–333.
Hill, R. I., Campbell, I. R., Davis, G. F., and Griffiths, R. W., 1992, Mantle plumes and continental tectonics: Science, v. 256, p. 186–193.
Hodges, K. V., and Spear, S. F., 1982, Geothermometry, geobarometry and Al_2SiO_5 triple point at Mt. Moosilauke, New Hampshire: American Mineralogist, v. 67, p. 1118–1134.
Hoisch, T. D., 1989, A muscovite–biotite thermometry: American Mineralogist, v. 74, p. 565–572.
Holland, T., and Blundy, J., 1994, Non-ideal interactions in calc amphibole and their bearing on amphibole–plagioclase thermometry: Contributions to Mineralogy and Petrology, v. 116, p. 433–447.
Hsü, K., Li, J., Chen, H., Wang, Q., Sun, S., and Sengör, A. M. C., 1990, Tectonics of South China: key to understanding west Pacific geology: Tectonophysics, v. 183, p. 9–39.
Hsü, K., Sun, S., Li, J., Chen, H., Pan, H. P., and Sengör, A. M. C., 1988, Mesozoic overthrust tectonics in south China: Geology, v. 16, p. 418–421.
Hu, X. J., 1991, The Precambrian geology of southwestern Zhejiang Province: Precambrian Geology, v. 5, p. 1–208 (in Chinese).
Hu, Z. Z., 1984, Structural analysis of the metamorphic rocks around Xishitun area, Zhenghe County, Fujian Province: Fujian Geology, v. 3, p. 33–46 (in Chinese).
Huang, H., 1989, Sm–Nd isotopic geochronology of Pingtan–Nanao metamorphic belt and its tectonic implications: Fujian Geology, v. 8, p. 12–24 (in Chinese).
Huang, J. Q., 1977, The basic outline of China tectonics: Acta Geologica Sinica, v. 52, p. 117–135 (in Chinese).
Jahn, B. M., Zhou, X. H., and Li, J. L., 1990, Formation and tectonic evolution of Southeastern China and Taiwan: isotopic and geochemical constraints: Tectonophysics, v. 183, p. 145–160.
Kretz, R., 1983, Symbols for rock-forming minerals: American Mineralogist, v. 68, p. 277–279.
Li, F. X., Ni, X. W., Hu, Z. X., and Yuan, Z. X., 1987, Ages and stratigraphic classification of the Kongling Group in the north side of the Huangling faulted dome: Hubei Geology, v. 3, p. 43–56 (in Chinese).
Li, G. K., 1988, A discussion on the ages of basement rocks in Fujian Province: Fujian Geology, v. 7, p. 80–118 (in Chinese).
——— 1989, Isotopic ages of the basement rocks in Fujian Province and their implications for regional tectonic evolution: Fujian Geology, v. 8, p. 159–168 (in Chinese).
Li, Q., and Leng, J., 1987, The upper Precambrian in Shenlongjia region: Tianjin, Tianjin Science and Technology Press, 503 p (in Chinese).
Li, X., 1994, A comprehensive U–Pb, Sm–Nd, Rb–Sr and ^{40}Ar–^{39}Ar geochronological study on Gueidong granodiorite, southeastern China: records of multiple tectonothermal events in a single pluton: Chemical Geology, v. 115, p. 283–295.
——— 1999, U–Pb zircon ages of granites from the southern margin of Yangtze Block and timing of Neoproterozoic Jinning Orogeny in SE China: Termination of Rodinia Assembly?: Precambrian Research, in press.
Li, X., Gui, X., and Yu, J., 1992, Sm–Nd and zircon U–Pb isotopic constraints on the age of formation of the Precambrian crust in southeastern China: Chinese Journal of Geochemistry, v. 11, p. 111–120 (in Chinese).
Li, Z. X., 1998, Tectonic history of the Major East Asian lithospheric blocks since the mid-Proterozoic–A synthesis, *in* Flower, editor, Mantle Dynamics and plate interactions in East Asia, AGU Geodynamic Series, v. 27, p. 221–243.
Li, Z. X., Li, X. H., Kinny, P. D., and Wang, J., 1999, 830-820 Ma Mafic to felsic igneous activity in South China: Part of Plume-induced rifting that led to the breakup of Rodinia?: Journal of Conference Abstracts, v. 4, p. 117.

Li, Z. X., and Powell, C. McA., 1999, Palaeomagnetic study of Neoproterozoic glacial rocks of the Yangtze Block: palaeolatitude and configuration of South China in the late Proterozoic Supercontinent–Discussion: Precambrian Research, v. 94, p. 1–5.
Li, Z. X., Zhang, L., and Powell, C. McA., 1995, South China in Rodinia: part of the missing link between Australia–East Antarctica and Laurentia?: Geology, v. 23, p. 407–410.
——— 1996, Positions of the East Asian cratons in the Neoproterozoic Supercontinent Rodinia: Australian Journal of Earth Sciences, v. 43, p. 593–604.
Ma, R., and Wang, A., 1994, Tectonic outline of Late Proterozoic collisional orogenic belt in South China: Anhui Geology, v. 4, p. 14–22 (in Chinese).
Mäder, U. K., and Berman, R. G., 1992, Amphibole thermobarometry: a thermodynamic approach: Current Research, Part E, Geological Survey of Canada, Paper, v. 92–1E, p. 393–400.
McMullin, D., Berman, R. G., and Greenwood, H. J., 1991, Calibration of the SGAM thermobarometer for pelitic rocks using data from equilibrium experiments and natural assemblages: Canadian Mineralogist, v. 29, p. 889–908.
Metcalfe, I., 1996, Gondwanaland dispersion, Asian accretion and evolution of eastern Tethys: Australian Journal of Earth Sciences, v. 43, p. 605–623.
Mezger, K., Bohlen, S. R., and Hanson, G. N., 1990, Metamorphic history of the Archean Pikwitonei Granulite Domain and the Cross Lake Subprovince, Superior Province, Manitoba, Canada: Journal of Petrology, v. 31, p. 483–517.
Pattison, D. R. M., and Tracy, R. J., 1991, Phase equilibria and thermobarometry of metapelites, *in* Kerrick, D. M., editor, Contact metamorphism: Mineralogical Society of America, Reviews in Mineralogy, v. 25, p. 105–206.
Plyusnina, L. P., 1982, Geothermometry and geobarometry of plagioclase–hornblende bearing assemblages: Contributions to Mineralogy and Petrology, v. 80, p. 140–146.
Powell, R., and Holland, T. J. B., 1990, Calculated mineral equilibria in the pelitic system, KFMASH (K_2O–FeO–MgO–Al_2O_3– SiO_2–H_2O): American Mineralogist, v. 75, p. 367–380.
Powell, R., Holland, J. T. B., and Worley, B., 1998, Calculated phase diagrams involving solid solutions via non-linear equations, with examples using THERMOCALC: Journal of Metamorphic Geology, v. 16, p. 577–588.
Preiss, W. V., Belperio, A. P., Cowley, W. M., and Rankin, L. R., 1993, Neoproterozoic, *in* Drexel, J. F., Preiss, W. V., and Parker, A. J., editors, The geology of South Australia: Precambrian: Bulletin–Geological Survey of South Australia, v. 54, p. 170–203.
Sandiford, M., and Powell, R., 1986, Deep crustal metamorphism during continental extension: ancient and modern examples: Earth Planetary Science Letter, v. 79, p. 151–158.
Sharp, Z. D., and Essene, E. J., 1991, Metamorphic conditions of an Archean core complex in the Northern Wind River Range, Wyoming: Journal of Petrology, v. 32, p. 241–273.
Shui, T., 1987, Tectonic framework of the southeastern China continental basement: Scientia Sinica, v. B30, p. 414–422 (in Chinese).
Spear, F. S., and Cheney, J. T., 1989, A petrogenetic grid for pelitic schists in the system SiO_2–Al_2O_3–FeO–MgO– K_2O–H_2O: Contributions to Mineralogy and Petrology, v. 101, p. 149–164.
Symmes, G. H., and Ferry, J. M., 1992, The effect of whole-rock MnO content on the stability of garnet in pelitic schists during metamorphism: Journal of Metamorphic Geology, v. 10, p. 221–237.
Thompson, A. B., 1976, Mineral reactions in the pelitic rocks: II. Calculations of some P–T–X (Fe–Mg) phase relations: American Journal of Science, v. 276, p. 425–454.
Thompson, A. B., and England, P. C., 1984, Pressure-temperature-time paths of regional metamorphism, II. Their influences and interpretation using mineral assemblages in metamorphic rocks: Journal of Petrology, v. 25, p. 929–955.
Thompson, J. B. Jr., 1957, The graphic analysis of mineral assemblages in pelitic schists: American Mineralogist, v. 42, p. 842–858.
Vernon, R. H., 1996, Problems with inferring P–T–t paths in low-P granulites facies rocks: Journal of Metamorphic Geology, v. 14, p. 143–154.
Wingate, M. T. D., Campbell, I. H., Compston, W., and Gibson, G. M., 1998, Ion microprobe U-Pb ages for Neoproterozoic basaltic magmatism in south central Australia and implications for breakup of Rodinia: Precambrian Research, v. 87, p. 135–159.
Wells, P. R. A., 1980, Thermal models for magmatic accretion and subsequent metamorphism of continental crust: Earth and Planetary Science Letter, v. 46, p. 253–265.
Wang, H. Z., and Mo, X. X., 1995, An outline of the tectonic evolution of China: Episodes, v. 18, p. 6–16.
Wang, H. Z., and Qiao, X., 1984, Proterozoic stratigraphy and tectonic framework of China: Geological Magazine, v. 121, p. 599–614.
Wu, M. D., 1988, Pre-Sinian mineralization in South Sichuan-Central Yunnan region: Jiangxi Geology, v. 2, p. 251–254 (in Chinese).
Wu, S., 1979, A study on isotopic geochronology of Late Proterozoic Bendong intrusives, Guangxi, China: Geochimca, v. 8, p. 187–194 (in Chinese).
Xu, B., 1992, Proterozoic terranes and polyphase collisional orogens in Anhui, Zhejiang, Jiangxi provinces: Beijing, Geological Publishing House, 112 p (in Chinese).
Xu, B. T., and Shui, T., 1988, Isotopic geochronology of paleobasement metamorphic rocks in Zhejiang and Fujian provinces: Jiangxi Geology, v. 2, p. 16–17 (in Chinese).
Yang, M. G., 1988, Meso- and Neoproterozoic stratigraphy, sedimentary formation and tectonic evolution of South China: Jiangxi Geology, v. 2, p. 112–121 (in Chinese).
Yang, M. G., and Fan, C. J., 1994, Tectonic framework of China, *in* Cheng, Y. Q., editor, Introduction to the regional geology of China: Beijing, Geological Publishing House, p. 448–466 (in Chinese).

Yao, Z. B., and Wei, X. J., 1994, Stratigraphy of South China, *in* Cheng, Y. Q., editor, Introduction to the regional geology of China: Beijing, Geological Publishing House, p. 313–340 (in Chinese).
Yie, B. D., 1990, Timing of the Baoban Group and gold mineralization in Dongfangerjia area, Hainan Island: Journal of Geological Exploration, v. 5, p. 12–17 (in Chinese).
Yuan, H. H., 1985, Archean age information in Dukou area, Sichuan, China: Journal of Chengdu College of Geology, v. 12, p. 79–84 (in Chinese).
Zhang, J. H., 1994, Metamorphic rock series and belts of South China, *in* Cheng, Y. Q., editor, Introduction to the regional geology of China: Beijing, Geological Publishing House, p. 364–367 (in Chinese).
Zhang, Q. R., and Piper, J. D. A., 1997, Paleomagnetic study of Neoproterozoic glacial rocks of the Yangtze Block: paleolatitude and configuration of South China in the Late Proterozoic Supercontinent: Precambrian Research, v. 85, p. 173–199.
Zhao, G. C., and Sun, D. Y., 1996, Polyphase metamorphic garnets from the Mayuan Group and their tectonic implications: Journal of Changchun University of Earth Sciences, v. 26, p. 34–42 (in Chinese).
Zhao, G. C., Sun, D. Y., and He, T. X., 1994a, Metamorphism and crustal evolution of the basement in the southeastern China: Beijing, Seismological Press, 131 p (in Chinese).
——— 1994b, P–T–D path of the Chencai Group: Journal of Changchun University of Earth Sciences, v. 24, p. 244–254 (in Chinese).
——— 1996, Buffering of metamorphic reaction temperature by metamorphic fluids in Mayuan Group, Northern Fujian Province: Acta Petrologica Sinica, v. 12, p. 59–69 (in Chinese).
Zhao, G. C., Wilde, S. A., Cawood, P. A., and Lu, L. Z., 1998, Thermal evolution of Archean basement rocks from the eastern part of the North China craton and its bearing on tectonic setting: International Geology Review, v. 40, p. 706–721.
——— 1999, Thermal evolution of two textural types of mafic granulites in the North China craton: evidence for both mantle plume and collisional tectonics: Geological Magazine, v. 136, in press.
Zhao, X., Coes, R. S., Gilder, S. A., and Frost, G. M., 1996, Paleomagnetic constraints on the paleogeography of China: implications for Gondwanaland: Australian Journal of Earth Sciences, v. 43, p. 643–672.
Zhou, X., Hu, S., Ren, S., and Li, J., 1993, Geochronological constraints on multistage tectonic evolution of the continental crust in southeastern China, *in* Li, J., editor, Geophysical structure and geological evolution of continental lithosphere in southeastern China: Beijing, Metallurgical Industry Press, p. 69–77 (in Chinese).
Zhu, Z. G., 1985, A discussion on structural history and stratigraphy of metamorphic rocks in Taxia–Guoyuan area, Nanping: Fujian Geology, v. 4, p. 23–40 (in Chinese).